nature communications

Article

https://doi.org/10.1038/s41467-026-71458-0

Early differential impact of MeCP2 mutations on functional networks in Rett syndrome patient-derived human cortical organoids

Received: 16 September 2024

Accepted: 17 March 2026

Published online: 14 April 2026

Check for updates

A list of authors and their affiliations appears at the end of the paper

Human cerebral organoids derived from induced pluripotent stem cells can recapture early developmental processes and reveal changes involving neurodevelopmental disorders. Mutations in the X-linked methyl-CpG binding protein 2 (MECP2) gene are associated with Rett syndrome, and disease severity varies depending on the location and type of mutation. Here, we focused on neuronal activity in Rett syndrome patient-derived organoids, analyzing two types of MECP2 mutations—a missense mutation (R306C) and a truncating mutation (V247X)—using calcium imaging with three-photon microscopy. Compared to isogenic controls, we found abnormal neuronal activity in Rett organoids and altered network function based on graph theoretic analyses, with V247X mutations impacting functional responses and connectivity more severely than R306C mutations. These changes paralleled EEG data obtained from patients with comparable mutations. Labeling >/>DLX promoter-driven inhibitory neurons demonstrated differences in activity and functional connectivity of inhibitory and excitatory neurons in the two types of mutations. Transcriptomic analyses revealed HDAC2-associated impairment in R306C organoids and decreased $GABA_A$ receptor expression in excitatory neurons in V247X organoids. These findings demonstrate mutation-specific mechanisms of vulnerability in Rett syndrome and suggest targeted strategies for their treatment.

Rett syndrome (RTT) is a progressive neurodevelopmental disorder that is primarily caused by mutations in the X-linked gene encoding methyl-CpG binding protein 2 (MeCP2), and predominantly affects girls[1,2]. Symptoms typically first appear between 6 and 18 months of age, and include the loss of purposeful hand skills, decline of speech and social engagement, motor abnormalities, and cognitive impairments[3]. Disease severity can vary significantly between individuals due to the many variations of MeCP2 mutations (which include missense and nonsense/truncating mutations)[4–7]. While 863 unique mutations have been identified, eight mutations constitute >60% of documented cases[8,9].

MeCP2 can directly bind to DNA selectively through its N-terminal methyl-CpG binding domain (MBD), and recruits other co-repressors or coactivators, such as Sin3a, HDAC1, HDAC2, or CREB1, through its C-terminal transcriptional repression domain (TRD), resulting in the regulation of a large number of downstream genes[10,11]. In the past two decades, studies exploring mutations of the MBD (or using MeCP2 null *MeCP2*$^{-/-}$ and *Mecp2*$^{/Y}$ mice) have revealed effects of altered MeCP2 affinity to CpG binding regions and their consequences[12–14]. Compared to MeCP2 null and MBD mutations, the impact of a C-terminus mutation is considered to be milder. One such mutation, MeCP2[R306C], affects the NCoR-interaction domain (NID) within the TRD, but does not affect affinity to the CpG binding domain, abolishing interactions between the NCoRco-repressor complex and HDAC3[15,16]. Disease severity has also been linked to mutation type in addition to location in the gene[5]. One of the most common truncating mutations in the MBD,

e-mail: osaki@mit.edu; msur@mit.edu

MeCP2[R168X], has been associated with severe symptoms[17]. On the other hand, a frequent missense mutation also in the MBD, MeCP2[T158M], has been associated with lesser disease severity[18,19]. Overall, milder disease severity has been described in Rett patients carrying missense mutations, and the effects of the missense R306C mutation in the NID/TRD have been reported as less functionally deleterious compared to nonsense or truncating mutations in the TRD[12]. Understanding the relationship between the mutation types of MeCP2 and disease severity is important for understanding the molecular mechanisms underlying the pathology of RTT, as well as for developing targeted treatment strategies.

Cerebral organoids derived from human induced pluripotent stem cells have emerged as powerful experimental systems for their ability to recapitulate early human neurodevelopmental processes[20,21]. This in vitro approach allows us to expand our current understanding of development, which is mostly constructed from studies with human individuals, animal experiments with rodents, and conventional 2D cell cultures in vitro. Importantly, patient-derived organoids facilitate analyses of pathological mechanisms underlying not only anatomical alterations[22–24], but also their neuronal functionality and developmental dynamics[25]. The ability to prepare cerebral organoids from RTT patients with different mutation types offers the opportunity to directly study the effects of mutations on early developmental events, especially functional networks, and potentially relate disease severity to early occurring dysfunction.

In this study, we investigated how two different MeCP2 mutations −the 916 C > T/R306C missense mutation and 705delG/V247X truncating mutation, both located near each other in the TRD, with R306C in the NID and V247X just outside of it−differentially impact the structure and function of developing neuronal networks. We carried out imaging-based quantification of patient-derived cortical organoids carrying these two mutations and their isogenic controls using three-photon and two-photon microscopy, employing genetically encoded Ca^{2+} indicators (GCaMP6f and jRGECO1a) along with label-free third-harmonic generation (THG) imaging and additional labeling techniques to identify specific types of neurons. We analyzed the responses and functional connectivity of neurons, including that of inhibitory/excitatory neurons, in MeCP2 mutant and isogenic control organoids and discovered systematic differences in features between mutation types. Differences in connection patterns were also revealed by network-based analyses based on graph theory. Interestingly, these differences resembled changes observed in EEG data from human patients with comparable mutations, suggesting early developmental origins of brain-wide connectivity. scRNAseq and bulk RNAseq enabled the characterization of different gene expression patterns in the organoids, reinforcing the hypothesis that distinct molecular pathways were affected by different mutations. Specifically, these analyses indicated that inhibitory-to-excitatory connections (GABA-GABRA2/4 and neurexin-neuroligin complex) were affected in V247X organoids, whereas HDAC2 gene expression was altered in R306C organoids. These findings pointed to the potential insight of mutation-specific strategies for restoring functional responses, and the application of specific agents indeed rescued neuronal activity-based connectivity in the two types of organoid in RTT.

Results

Cerebral organoids derived from RTT patient-derived iPS cells show mutation-specific structural changes

Cerebral organoids were constructed from RTT patient-derived iPS cells carrying MeCP2[R306C] and MeCP2[V247X] mutations (Fig. 1a). Their isogenic pairs (iPS cells that have the same genetic information except for the MeCP2 mutation) were used as controls (Fig. S1A–D). The isogenic control for the MeCP2[R306C] mutation was created by CRISPR/Cas9 mutagenesis genome editing, and the isogenic control for MeCP2[V247X] was cloned and selected from patient iPS cells in which the X chromosome with the mutant MeCP2 allele was inactivated (Figs. 1b and S1). Wild-type MeCP2 and mutant MeCP2 expression in these four iPS lines were confirmed by site-specific PCR, western blotting, and immunostaining (Fig. S1E–G) (for detailed differentiation protocols, see Methods and Supplemental Information; Figs. S2A–C). Before starting differentiation into cerebral organoids, their pluripotency was confirmed by immunostaining with Oct 3/4, Nanog, TRA-1-60, and SSEA4 (Fig. S1H). During organoid differentiation (0–3 months), representative iPS markers, Nanog and Oct3/4, decreased, and neuronal progenitor marker SOX2 and neuron marker expression (DCX and TUJ1) increased (Fig. S2D, E). We performed scRNAseq and derived integrated UMAP plots from 3-month cultured organoids (with both R306C and V247X mutations and isogenic controls) to first identify their cell types and donor-dependent similarities and differences (Fig. 1c). These revealed multiple cell types (Figs. 1c and S3B), including neural progenitor cells (expressing *SOX2*), radial glia cells (RGCs, expressing *VIM*), neuronal cells (*DCX*), cycling RGCs (*ASPM*), outer RGCs (oRGCs; *HOPX*) and intermediate progenitor cells (IPCs; *EOMES*). MeCP2 was expressed in all cell types (Fig. S3C). We further identified excitatory neurons (expressing *GRIA2 and SATB2*) and inhibitory progenitors and neurons (expressing *ASCL1, GAD1*, and *GAD2*), as well as astrocytes (expressing *S100B* and *APOE*, Figs. 1e and S3D, E). UMAP plots confirmed multiple cell types in both R306C and V247X organoids (Fig. 1e, f, and highly-reduced expression of MeCP2 in V247X organoids, as expected (Fig. 1d). Cryosectioning showed that the diameters of V247X organoids were significantly larger than isogenic controls throughout the differentiation process, whereas no significant differences between R306C organoids and isogenic controls were observed (Figs. 1g and S2B, C). The number of rosette structures in V247X organoids was higher than in controls, while no differences were observed in R306C organoids (Figs. 1h and S2I). In addition, immuno-histological cryosectioning also revealed structural differences in the neuron layers (Fig. S2D, F, G): With immunostaining, V247X organoids exhibited a thinner CTIP2 layer and a thicker SATB2 layer than the isogenic controls, whereas R306C organoids did not show significant differences (Figs. 1i and Fig. S2G). After placing cultured organoids onto Matrigel-coated plates, the axonal thickness, migration distance, and axon length were quantified (Figs. S2J, K). V247X organoids showed significantly-reduced axon thickness and length, which implies slower maturation of neurons, while the R306C organoids showed reduced axon thickness compared to control. To assess potential escape from X chromosome inactivation, we performed GSEA using positional gene sets from the human MSigDB. We did not observe any significant enrichment or differential expression of genes specifically on the X chromosome between V247X organoids and isogenic control organoids (Fig. S3F, G). These findings demonstrate that a wide range of cell types is present in organoids with both kinds of mutation, and several structural features of organoids show mutation-specific differences.

Altered neuronal activity and synchronicity in RTT organoids

To examine neuronal activity at signal cell resolution, we utilized CAG-driven GCaMP6f, which was encapsulated with AAV and introduced into the organoids. Subsequently, these organoids were transferred into a custom-made microfluidic device for observation with a three-photon microscope (with imaging at 1300 nm) (Fig. 2a). The microfluidic device was designed for fixing the geometrical position of cerebral organoids, and a temperature feedback system allowed them to be kept at a steady temperature of 37 °C during imaging. The field of view, including target neurons in cerebral organoids, was determined based on the depth from the surface and the morphology of the neurons identified by THG label-free imaging[24] (Fig. 2b). Quantification of neuronal activity after deconvolution revealed significantly decreased average activity in R306C organoids compared to isogenic controls (Fig. 2–e). In V247X organoids, mean spike frequency

https://doi.org/10.1038/s41467-026-71458-0

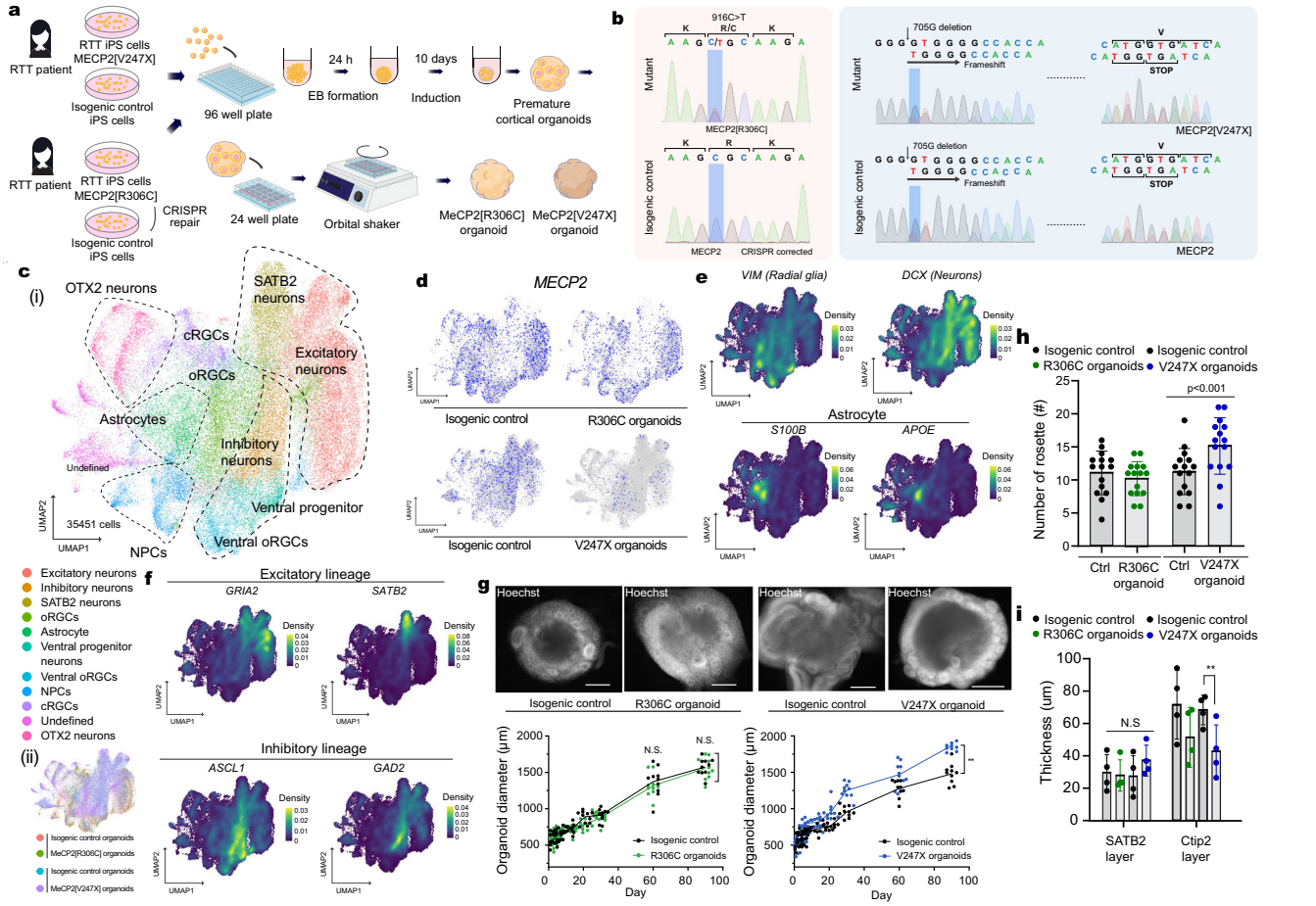

Fig. 1 | Engineering Rett syndrome patient-derived cortical organoids and characterization. a Schematic illustration of engineering and differentiating cortical organoids from human Rett syndrome patient-derived induced pluripotent stem cells (iPS cells). Two different MeCP2 mutations, [R306C] and [V247X], and their isogenic controls were studied. **b** Left, MeCP2[R306C]: Sanger sequencing confirmed the heterozygous mutation of 916 C > T in MeCP2 and homozygous expression of MeCP2 in both alleles of the X chromosome in isogenic control by CRISPR/Cas9 repairing. Right, MeCP2[V247X]: both mutant and isogenic control have 705 G deletion on one of the alleles in the X chromosome, leading to a frameshift mutation; however, the mutant allele in isogenic control iPS cells was inactivated, expressing only wild-type MeCP2. **c** (i) Integrated UMAP plot from four different types of organoids (MeCP2[R306C] and [V247X] and their isogenic controls) with cell-type annotations. Cells were pooled from eight individual organoids, with 35351 cells analyzed in total. (ii) UMAP plot label with four different genotypes. **d** Feature plots of MeCP2 expression. V247X organoids expressed no MeCP2, regardless of cell type. **e**, **f** Feature plots identifying cell types in organoids: radial glia (*VIM*), inhibitory radial glia (*ASCL1*), cortical excitatory neurons (*DCX, GRIA2, SATB2*), inhibitory neurons (*GAD2*), and astrocytes (*S100B* and APOE). **g** Cryosectioning of cortical organoids was used to characterize nuclear staining and quantification of organoid diameter, which increased up to 3 months. $n = 10$ organoids. $^{*}p < 0.05$, $^{**}p < 0.01$; one-way ANOVA. Data are presented as mean values ± SD. Scale bars: 500 μm. **h**, **i** Comparisons of number of rosette structures and the thickness of *CTIP2* and *SATB2* layer by immunostaining (see Fig. S2g, h). $n = 15$ organoids (**h**) and four organoids (**i**). $^{**}p < 0.01$; one-way ANOVA. **h**, **i** Data are presented as mean values ± SD.

decreased slightly but significantly, similar to R306C organoids (Fig. 2c–e). In addition, pairwise correlations between neurons in organoids were also decreased in both mutations, suggesting that R306C and V247X mutations both had reduced synchronicity (Fig. 2c, f). Treatment with an antagonist of GABA receptors (bicuculline) increased spike activity in MeCP2[V247X] mutant organoids and isogenic controls (Fig. 2g). In all conditions, treatment with an antagonist of AMPA receptors (CNQX) and NMDA receptors (AP5), with/without bicuculline, suppressed neuronal activity (Fig. 2g). This result suggests that neurons in cortical organoids are hyperpolarized by GABA signaling. Taken together, cortical organoids with or without MECP2 mutations appear to have functional excitatory (glutamatergic) and inhibitory (GABAergic) synapses.

Differential impact on functional network architecture in RTT organoids

To analyze functional network architecture in cerebral organoids, we utilized methods based on graph theory[26] to examine multi-neuron Ca^{2+} imaging data (see Method sections). We hypothesized that the connectivity of neurons might be optimized to maximize the efficiency of information transfer[27], even in control organoids, and mutant organoids may exhibit inefficient connectivity. To estimate the functional connectivity between neurons and assess their efficiency, we first calculated Pearson's correlation coefficients between single neuron fluctuations over time (Figs. 2c and 3ai). Each neuron, represented by its deconvolved ΔF/F Ca^{2+} signal, was treated as a network node. A correlation matrix was constructed by concatenating all pairwise correlations between nodes and thresholds to transform the continuous association matrix into a binary adjacency matrix (Fig. 3ai)[26]. Then, graph network models were constructed in two ways: (a) a structural network that retained the spatial information of neurons (Fig. 3aii), and (b) a functional network that emphasized topological properties derived from pairwise correlations (such that neurons with higher correlations were situated closer together, leading to clustering), abstracting away from the physical arrangement of neurons to focus on interactions[28,29] (Fig. 3aiii).

https://doi.org/10.1038/s41467-026-71458-0

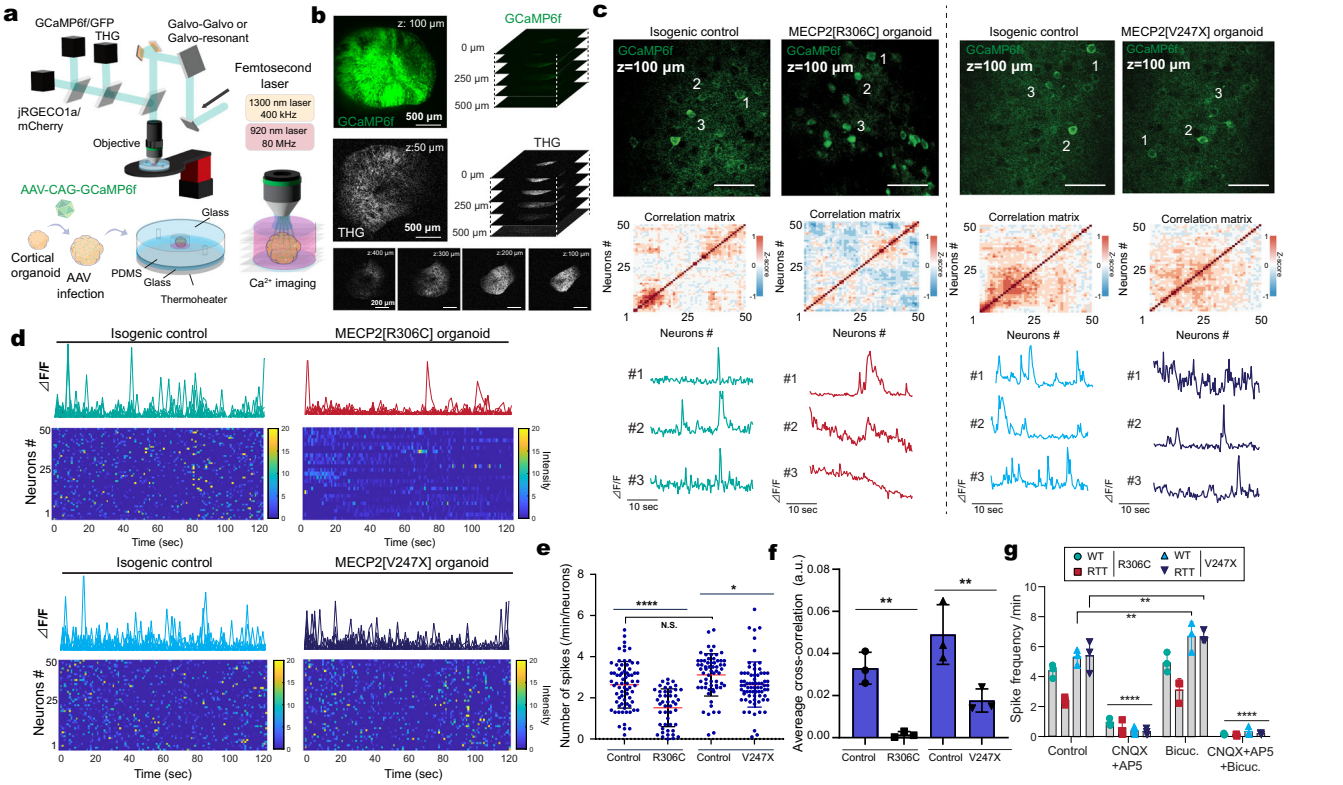

Fig. 2 | Functional analysis of cortical organoids by Ca^{2+} imaging. a Cortical organoids at 3 months were infected by AAV-CAG-GCaMP6f for Ca^{2+} imaging. Cortical organoids were placed in a custom microfluidic device to fix the organoid's position and prevent movement during the imaging and observation duration. Time-series data with Ca^{2+} imaging were taken with a three-photon microscope at 1300 nm by scanning a galvo-galvo mirror. **b** Z-slice images of GCaMP6f and label-free third-harmonic generation (THG) imaging. THG allows us to determine the structure of organoids. **c** Ca^{2+} signals from representative single neurons ($n = 5$ neurons each, at ~100 µm depth) from MeCP2[R306C] and [V247X] organoids and their isogenic control organoids. The correlation matrix shows the synchronized activity amongst the measured neurons in each field of view (FOV). Both mutant organoids exhibited reduced pair-wise correlation among their neurons. **d** Raster plot of activity derived from a larger number of neurons in each FOV. **e** Quantification of spike frequency. Ca^{2+} imaging data were deconvolved to extract spike activity. $n = 47$ from five different organoids and 5 different FOV. No significant difference was found between isogenic controls in spike frequency, but there were differences between mutant and isogenic pairs. Data are presented as mean values ± SD. **f** Changes in the average pair-wise correlation between neurons. $n = 3$. $^{*}p < 0.05$, $^{****}p < 0.0001$; one-way ANOVA. Data are presented as mean values ± SD. **g** Treatment with CNQX and AP5 immediately suppressed the neuronal activity and quantification of spike frequency. Ca^{2+} imaging data in the presence of CNQX and AP5, bicuculine, and all three drugs (CNQX, AP5, bicuculine). Treatment with bicuculline alone slightly but significantly increased spike frequency in MeCP2[V247X] mutant organoids and isogenic controls, consistent with countering the functional effects of GABAergic inhibition. $n = 3$. $^{*}p < 0.05$, $^{**}p < 0.01$; one-way ANOVA. Data are presented as mean values ± SD.

First, we counted the number of connections for each node (Fig. 3a, b) (referred to as its "degree", with the distribution of the degree across all nodes referred to as the "degree distribution"). The degree distribution for different organoids indicated distinct connectivity profiles, indicating differences in the extent to which neurons were connected to neighboring neurons. For R306C organoids, the amplitude and geometric mean of the distribution (fitted with a chi-square distribution) exhibited a higher value compared to controls, indicating a greater number of connections per neuron. For V247X organoids, the amplitude and geometric mean of the distribution were small and similar to controls. However, a few nodes had a very large degree, indicating the existence of so-called "hub" neurons that made significantly more connections than the others[30,31]. The distribution (fitted with a sum of two Lorentzian distributions) reflected a significant number of highly-connected hub neurons. The architecture of the functional network across recorded neurons for R306C and V247X organoids (Fig. 3c) was used to derive the local clustering coefficient, which was larger in R306C organoids than in isogenic controls (comparing 'empirical' or experimentally-observed coefficients with 'shuffled'), indicating more local clustering of coactive neurons (Fig. 3d). For V247X organoids, in contrast, no significant difference in local clustering coefficient was observed compared to controls. To obtain a quantitative measure of functional network architecture, we calculated their small-world propensity (SWP), a parameter combining local clustering with path lengths: high SWP relative to shuffled indicates higher clustering and shorter path length, and is usually consistent with more efficient information segregation and integration[26]. Our results showed that both R306C and V247X mutations affected SWP: SWP was significantly decreased in R306C organoids compared to controls, but slightly increased in V247X organoids, whereas SWPs in isogenic controls were equivalent (Fig. 3e).

Each organoid rosette and its associated ventricular zone may reflect the precursor of a cerebral hemisphere[32]. SWP is a measure of network organization that can be applied across scales[26,27] and its conceptual applicability has been shown in in vitro iPS-derived neurons on a multielectrode array (60 electrodes) to evaluate their SWP and hub structure, or modularity[33]. Thus, we next asked whether alterations of network structure in organoids represented changes in cortical organization that could also be discerned in human RTT patients. EEGs were recorded from the scalp surface of five RTT patients with two types of truncating mutations in the TRD, MeCP2[R255X] and [R270X], and the missense MeCP2[R306C] mutation in the NID, along with age-matched controls (Fig. S4). EEG data were analyzed with graph theoretic approaches based on wavelet

https://doi.org/10.1038/s41467-026-71458-0

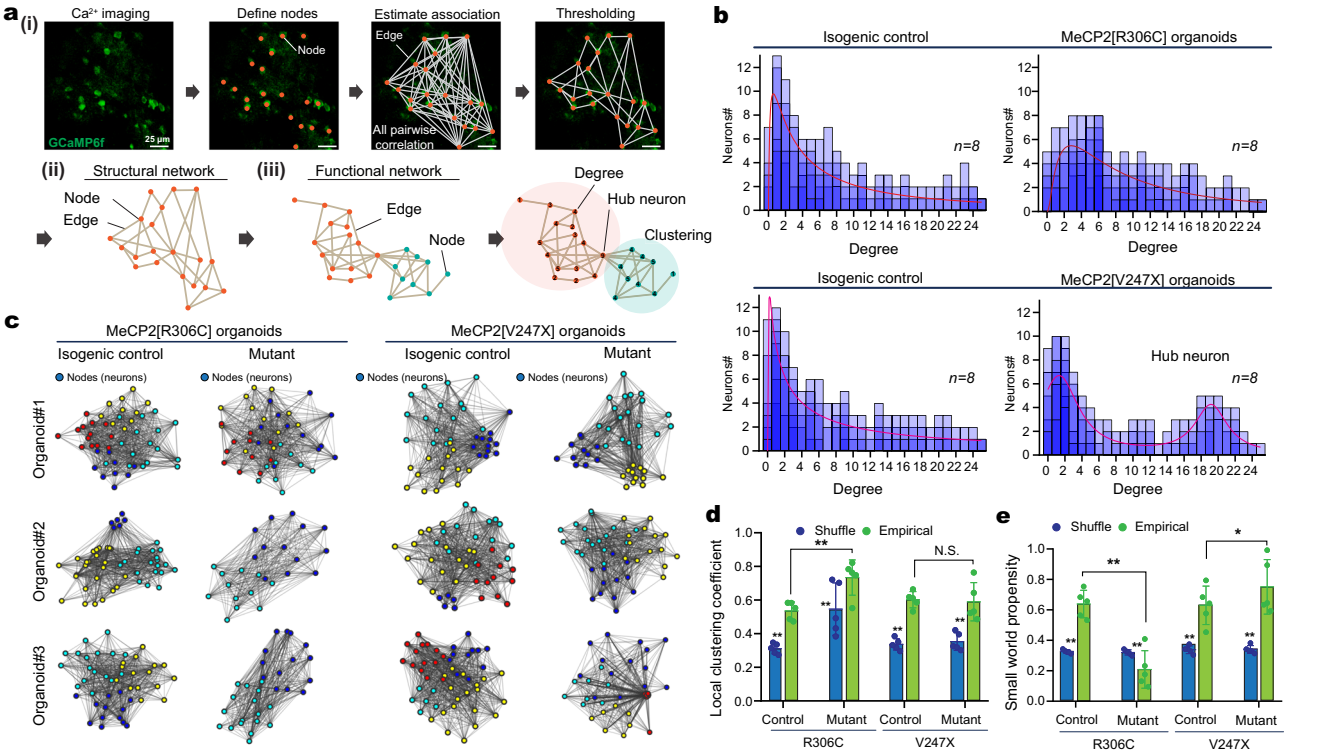

Fig. 3 | Network analysis of organoids. a Scheme of functional and structural topological analysis based on graph theory. Individual neurons were identified as nodes, nodes were connected to form edges according to the pairwise correlation between neurons, the connections (edges) were thresholded, and the results were plotted with geometric or neuron location information (as 'structural network') or with topological information (as 'functional network'). The connection degree, hub neurons, local clustering coefficient, and path length were characterized. **b** Degree distribution of MeCP2 mutant [R306C] and [V247X] and isogenic control organoids. Degree distributions were fitted with a chi-square curve in R306C and both sets of control organoids. The V247X organoid distribution was fitted with a sum of two Lorentzian distributions. $n = 8$. **c** Plots of functional network maps in topological space; three representative organoids. Colored nodes represent neurons that belong to the same cluster. **d** Quantified result of local clustering coefficient. 'Empirical' denotes data from actual time series used for correlation calculation. 'Shuffle' denotes randomly shuffled data as a control. $n = 5$ $^{*}p < 0.05$, $^{**}p < 0.01$; one-way ANOVA. Data are presented as mean values ± SD. **e** Small-world propensity calculated using the local clustering coefficient and path length. $n = 5$. $^{*}p < 0.05$, $^{**}p < 0.01$; one-way ANOVA. Data are presented as mean values ± SD.

coherence with specific frequency windows (Fig. S4A–C). Power spectrum density (PSD) analyses from the RTT patients showed variable changes across frequency bands in the cases with R255X and R270X mutations (Fig. S4C, D). In the case of a R306C mutation, PSD in beta-band frequency was significantly lower than in the control, consistent with previous findings[34]. Similar to organoids, we analyzed the connectivity between different brain regions based on graph theory (Fig. S5A–C). Cases with R255X and R270X mutations showed roughly similar correlations between multiple brain regions compared to controls, whereas brain activity in the Rett patient with the R306C mutation appeared to be more strongly correlated across multiple brain regions compared to control (Fig. S5A). In addition, network structure defined by SWP (Fig. S5C) showed that SWP values of patients with truncating mutations were either slightly decreased compared to controls (R255X mutation) or slightly increased (R270X mutation). In contrast, SWP values in the patient with a R306C mutation were strongly decreased compared to the control. This trend is consistent with the data from cortical organoids with the R306C mutation (Fig. 3e). While based on a limited number of subjects, these preliminary analyses suggest that some large-scale patterns of connectivity changes discerned in RTT patients may have their roots in early stages of development.

Finally, using cortical organoids, we examined whether the disposition of connections (i.e., their spatial orientation or direction) was affected by RTT mutations. Three-photon simultaneous Ca^{2+} imaging and label-free THG imaging enabled the determination of layer structures within organoids and the measurement of neuronal activity across the superficial, intermediate, and SVZ/VZ layers (Fig. 4a). This layer-specific information was subsequently incorporated into the analysis of neuronal activity based on Ca^{2+} imaging. The analyses revealed significant suppression of neurons in the intermediate layer in both kinds of mutant organoids compared to isogenic controls, with no significant differences observed in the neurons of the superficial and SVZ/VZ layers (Fig. 4b). Additionally, we examined whether interneuronal correlations were differentially influenced by the location of neurons within layers or across inter-layer zones. We calculated pairwise correlations and related them to the angle (θ) formed by the line connecting the two neurons and the line connecting one neuron and the center of the rosette-like structures (thus, θ values would be high for intra-layer pairs and low for inter-layer pairs, and cos θ would vary from 0 to 1, respectively) (Fig. 4c, d). Our findings indicate that neurons within the same layer tend to exhibit stronger connectivity than those in different layers across all conditions. However, these trends became less pronounced in RTT mutant organoids, particularly in the case of the V247X mutation (Fig. 4d, e). Thus, RTT mutations alter the spatial disposition of neuronal connections during development in addition to their number, strength, and SWP.

Altered gene expression in RTT organoids and the impact of specific genes in R306C and V247X mutations

Changes in functional networks and architecture following Rett mutations may reflect differential gene expression patterns in mutant organoids compared to controls. To identify such changes and their potential impact, we performed bulk RNAseq followed by differential

https://doi.org/10.1038/s41467-026-71458-0

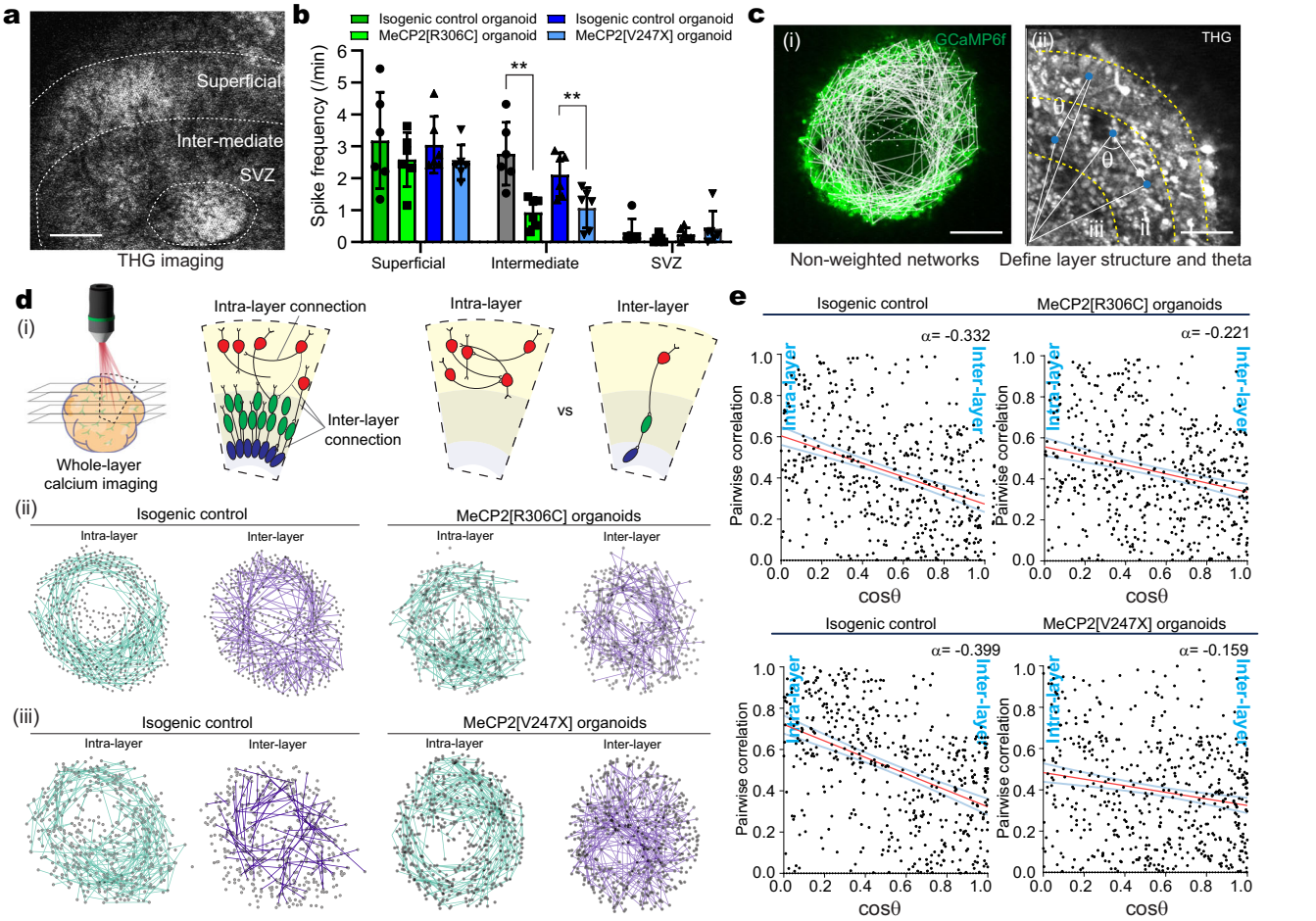

Fig. 4 | Layer-specific neuronal activity and laminar connectivity analysis of neurons in cortical organoids. a THG imaging facilitates the determination of the layer structure in organoids. Scale bar: 50 µm. **b** Spike frequency in each layer was separately calculated based on categorical information about the layer. $n = 6$. $^{**}p < 0.01$; one-way ANOVA. Data are presented as mean values ± SD. **c** Conceptual images for defining the layer structure by THG imaging and inter/intra layer connection by calculating the angle (θ) toward the edges from the center of the VZ layer. Scale bar: (i) 200 µm and (ii) 50 µm. **d** (i) Whole-layer calcium imaging to identify intra-layer connectivity and inter-layer connectivity. (ii) Representative intra-layer and inter-layer neuronal networks of MeCP2[R306C] mutant cortical organoids and isogenic control organoids. (iii) Representative intra-layer and inter-layer neuronal networks of MeCP2[R306C] mutant cortical organoids and isogenic control organoids. **e** Relationship between the angle between neurons and their pairwise correlation. Neurons in the same layer tended to be more connected than in different layers in all conditions; however, these trends become weaker in RTT mutant organoids, especially MeCP2[V247X] mutant organoids. Pooled from individual four organoids. $n = 4$.

gene expression analysis, and derived integrated UMAPs with isogenic control and mutant organoids from the same donor, isolated from 3-month cultures (Fig. 5, dataset itself is reproduced from Fig. 1c). UMAPs from organoids with the R306C mutation and isogenic controls specified multiple subtypes of neurons, as well as radial glia and astrocytes (Fig. 5a). We identified excitatory neurons which express *DCX, BCL11A, BCL11B, GRIN2B, GRIN2A, FOXG1, FOXP2, SATB1, SATB2* (see Methods section). In addition, we confirmed inhibitory lineage cells, which express *DLX1, DLX2, DLX5, DLX6, GAD1, GAD2* (see Methods section, Fig. 5a). The volcano plot from bulk RNAseq showed 343 upregulated genes and 107 downregulated genes compared to isogenic control organoids (Fig. 5b). One of the highest upregulated genes in R306C mutant organoids was *HDAC2* (Histone Deacetylase 2), one of the co-repressors of MeCP2. GO enrichment analysis revealed that the R306C mutation influenced pathways related to alteration of cellular components, such as the receptor complex, neuronal spine, and dendritic spine, as well as peptidyl-tyrosine modification and biogenesis, including proliferation and differentiation (Fig. S6A). scRNAseq revealed that the expression levels of HDAC2 tend to be altered in relatively mature excitatory and inhibitory neurons and astrocytes, but not in radial glial cells, even though all cell types expressed HDAC2 (Fig. 5c). To infer neuron-neuron communication with the scRNAseq dataset, NeuronChatDB[35,36] was employed and predicted altered pre-post synaptic connectivity, especially among excitatory neurons, inhibitory neurons, and astrocytes, along with decreased number of links between the cells and decreased strength of connections (Fig. 5e). Importantly, cell-adhesion complexes that support synaptic connections, especially components of the neurexin–neuroligin signaling pathway (e.g., *NRXN2-NLGN4X, NRXN2-NLGN1, NRXN1-NLGN4X*) and glutamate-glutamate receptor pathway, were deficient in mutant R306C organoids compared to control organoids (Fig. 5f).

In MeCP2[V247X] organoids, scRNAseq revealed fewer diverse and immature neuron and astrocyte subtypes compared to MeCP2[R306C] organoids and isogenic controls (Fig. 5g). This lack of diversity and maturity is consistent with immunostaining results and morphological characterization (e.g., CTIP2 layer thickness, Figs. 1 and Fig. S2G, H), which suggests donor-dependent differences in organoid development. As in R306C organoids, we found excitatory neurons that express FOXG1, SATB2, and Ctip2, and inhibitory lineage cells that express ASCL1 and GAD2. The mutation impacted a large number of genes (494 downregulated genes and 896 upregulated genes), as

shown in the volcano plot (Fig. 5h), influencing axonal development, the regulation of neuronal projection development, as well as the Wnt signaling pathway (Fig. S6B). Highly-downregulated genes included genes in the GABA-A receptor family (*GABARA2* and *4*, and *GABARE*), while highly-upregulated genes included *GRIN2A*, which encodes the GluN2A NMDA receptor subunit (Fig. 5h). scRNAseq further revealed the cell type-specific down-regulation of *GABRA2* and *GABRA4* (Fig. 5i), and upregulation of *GRIN2A* (Fig. S6C): these genes were regulated in only excitatory or immature excitatory neurons, but not inhibitory neurons. NeuronChatDB[36] was used to identify the loss of synaptic communication in mutant organoids (Fig. 5j), indicating that the number of links and strength of several neurexins–neuroligin and GABA-GABA receptor complex pathways were decreased (Fig. 5k). In particular, *NRXN1-NLGN4X*, *NRXN1-NLGN3X*, and *GABA-GABRA4* interactions were altered (Figs. 5k and S6D). The chord diagram revealed that *GABA* (pre-synaptic in inhibitory neurons)-*GABRA4* (post-synaptic in excitatory neurons) became weaker in V247X mutant organoids over control (Fig. 5l). To validate the predicted alterations in neuron–neuron communication inferred by NeuronChatDB, we examined the expression of key ligand–receptor genes across relevant cell types from scRNAseq data (Fig. S7). Violin plots confirmed differential expression patterns consistent with the computational predictions (Fig. S7), confirming downregulated gene expression of *NRXN1*, *NRXN3*, *NLGN4X* in inhibitory neurons and *NRXN1*, *NRXN3*, *NLGN4X* and *GABARA4* in excitatory neurons in V247X mutant organoids compared to isogenic controls (Fig. S7A). *NLGN4X* expression was decreased in inhibitory neurons, while *NRXN1* and *NRXN2* were downregulated in excitatory neurons (Fig. S7B). These transcriptional changes likely underlie the disrupted pre- and postsynaptic organization between excitatory and inhibitory neurons. Furthermore, immunostaining with super-resolution microscopy demonstrated reduced GABA receptor alpha-4, Neuroligin-4, Neurexin-1 expression in MeCP2[V247X] organoids compared to controls (Fig. S7C–E), supporting the computationally inferred disruption of inhibitory signaling.

Analysis of cell-cell communication using the scRNAseq dataset with CellChatDB[35] showed that the total number of interactions in all cell types was decreased in R306C organoids compared to control, but not in V247X organoids (Fig. S6E, F). The strength of communication was slightly decreased in both cases (Fig. S6G). We found that astrocytes played an important role in this dysregulation (Fig. S8). CellChatDB analysis of differential interactions (Fig. S7A–C) showed that, in R306C organoids, most intercellular communication was downregulated, and a few (NPC to oRGCs, ventral progenitor cells to ventral oRGCs, and ventral oRGCs to inhibitory neurons) were upregulated. In contrast, astrocyte-to-excitatory neuron and astrocyte-to-immature excitatory neuron communication in V247X organoids were selectively deficient (Fig. S8B). In particular, in V247X organoids, NRG3 (astrocyte)-ERBB4 (excitatory, astrocyte and radial glia, and NPC), NRXN3 (astrocyte)-NLGN1 (excitatory neurons, immature excitatory neurons), and Glu-SLC1A2/3-GLS to GRIAs, intercellular communication was significantly reduced, but not in R306C organoids (Fig. S8D–G). Both NRG3-ERBB4 and Glu-SLC1A2/3-GLS to GRIAs signaling pathways are fundamental functions of astrocytes, necessary for forming astrocyte-neuron adhesion and regulating glutamate uptake at glutamatergic synapses[37–39]. In astrocytes, the expression of the ligand Neuregulin 3 (NRG3) and the glutamate-metabolizing enzyme Glutaminase (GLS) was significantly reduced in MeCP2[V247X] organoids, suggesting a potential disruption in glutamate homeostasis, while SLC1A2, SLC1A3, and the receptor ERBB4 showed no significant changes. In summary, the downregulation of NRG3 and GLS in astrocytes, together with decreased ERBB4 expression in both inhibitory and excitatory neurons, likely underlies the dysregulation of the NRG3(astrocyte)–ERBB4(neuron) and Glu–SLC1A2/3-GLS–GRIA signaling pathways predicted by CellChatDB. Thus, these analyses suggest mutation-specific roles for astrocytes in the pathophysiology of RTT.

The neuronal gene expression findings demonstrating HDAC2 upregulation in R306C organoids and GABA-A receptor downregulation in V247X organoids led us to examine whether HDAC2 inhibition or GABA activation would rescue neuronal activity or connectivity in these mutant organoid types. Thus, a selective inhibitor of HDAC2 (CAY10683) and a GABA agonist (Baclofen) were administrated to 3-month cultured organoids for 72 hours (Fig. 5m). The HDAC2 inhibitor increased neuronal activity and restored SWP to control levels in R306C organoids, without causing any change in V247X organoids (Fig. 5n, o), while 24-hour treatment did not show significant restoration of neuronal activity and 7 days treatment caused significant morphological change along with disintegration of spherical organoids structure and the loss of neuronal activity (Fig. S10A, B). Baclofen treatment generally reduced the level of neuronal activity in all organoid types (Fig. 5n). In V247X organoids, it also reduced SWP, restoring it to control levels, while it caused no change in R306C organoids (Fig. 5o). Thus, specific gene expression changes may underlie neuronal activity levels and functional architecture in different RTT mutations, and selective application of molecules that counter these changes may be plausible mechanisms for restoration of function.

These results indicate that other missense vs truncating mutations may affect gene expression, neuronal activity, and network function, potentially through shared as well as unique context-dependent MeCP2 mechanisms. Analysis of differential and shared gene expression in R306C and V247X mutant organoids identified 229 shared dysregulated genes by bulk RNAseq (Fig. S3H). These included upregulated genes and pathways (e.g., RNA polymerase II-specific, DNA-binding transcriptional activation, voltage-gated sodium channel complexes), as well as downregulated pathways (e.g. G protein–coupled peptide receptor activity and GABAergic synapses (Fig. S3I, J). These findings suggest both mutation-specific and convergent roles of MeCP2 dysfunction.

Co-DLX labeling with Ca2+ imaging to identify functional connectivity in excitatory and inhibitory neurons

The transcriptome analysis above revealed that V247X mutant organoids displayed significant alterations in the development of GABAergic synaptic connectivity. In addition, scRNAseq results represented the population of inhibitory neurons marked by *GAD2*, and various subtypes of interneurons (*SST, VIP*, and *PVALB*-expressing neurons (Fig. S3C, K, L, M). To follow up on these findings, GABAergic interneurons expressing DLX were dual-labeled with EGFP and a red Ca^{2+} tracer (jRGECO1a). This dual labeling enabled a comparative assessment of the activity of excitatory and inhibitory neurons individually, as well as their functional connectivity (Figs. 6a–c and S11E). First, flow cytometry and cell sorting were performed to confirm the population of DLX-positive cells, followed by gene expression analysis (Fig. 6a and S11A–D). Flow cytometry and imaging-based counting analyses revealed that, in all types of organoids, DLX-positive cells constituted ~15% of the total cells, indicating the presence of GABAergic interneurons (Fig. S11C). There were no significant differences in the ratio of excitatory to inhibitory neurons among the different types of organoids. The remaining 85% of cells were considered as putative excitatory neurons. Utilizing functional connectivity information from DLX labeling allowed us to define the node connectivity in functional networks of excitatory and inhibitory neurons (Fig. 6c, d). The spike frequency of inhibitory neurons tended to be higher than that of excitatory neurons (Fig. 6e). Network models of organoid networks revealed that the nodes of inhibitory neurons in all organoid conditions were connected to numerous nodes of excitatory neurons in the graph, resulting in the formation of one or two modules of networks (Figs. 6d and S11F–H). In V247X organoids, E-I/inhibitory-excitatory connectivity exhibited reduced strength, while excitatory-excitatory connectivity increased in relative strength compared to

https://doi.org/10.1038/s41467-026-71458-0

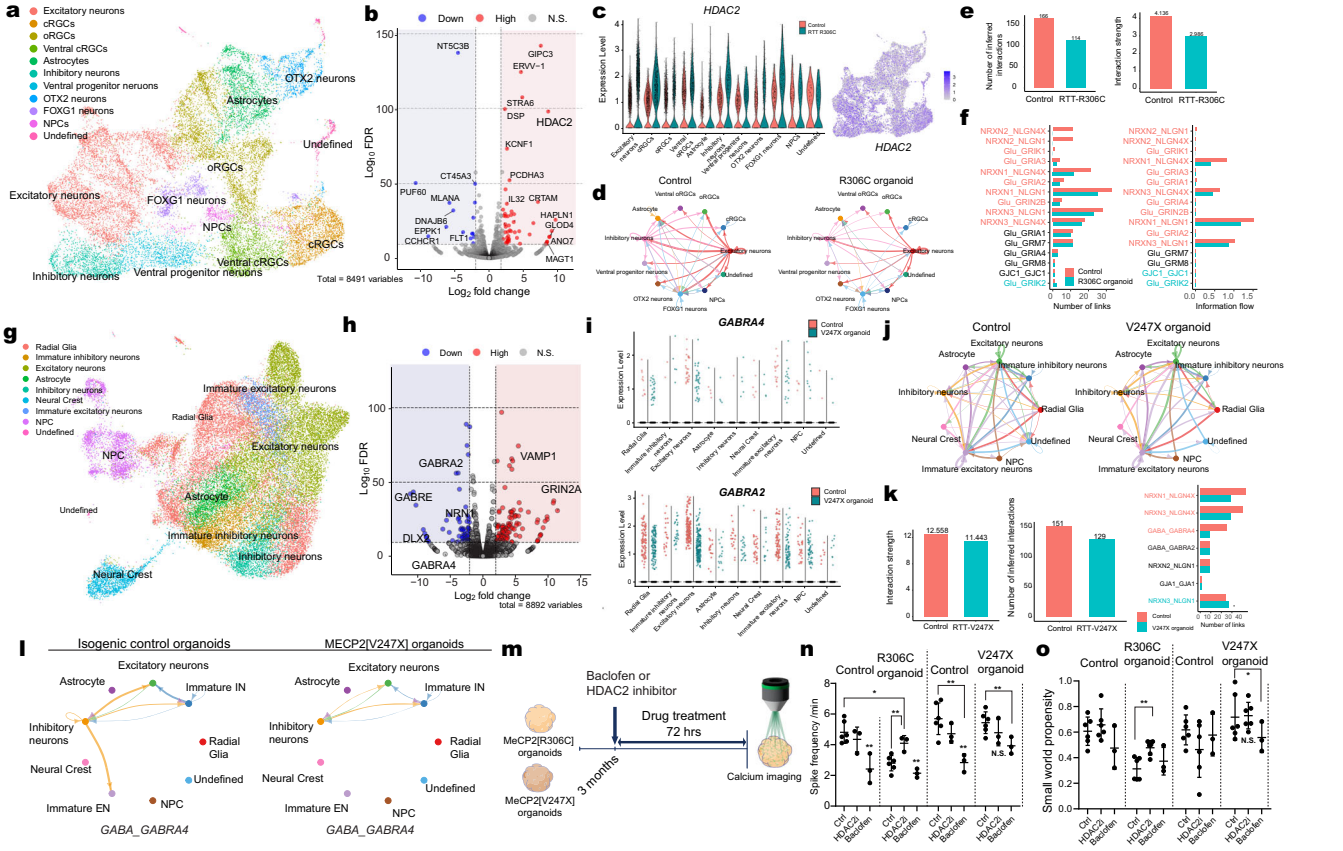

Fig. 5 | Differential gene expression in mutant organoids defined by bulk RNAseq and scRNAseq. a Integrated UMAP plot of 3-month cultured RTT-R306C cerebral organoid and isogenic control, identifying the cell types of organoids. Data are reproduced from Fig. 1C. **b** Differential gene expression in cortical organoids carrying MeCP2[R306C] mutation, identifying HDAC2 overexpression in the mutant organoids. RNA was extracted and pooled from eight different 3-month organoids in each condition for bulk RNAseq. The volcano plot shows 343 upregulated and 107 downregulated genes from bulk RNAseq. **c** HDAC2 expression after classifying cell types with scRNAseq. Altered HDAC2 gene expression was observed in all neural cells, including excitatory and inhibitory neurons, radial glia, and astrocytes. **d** Neuron-neuron connectivity inferred by NeuronChatDB in R306C mutant and control organoids. **e** Quantification of differential inferred neuron-neuron interaction. **f** Significant downregulated/upregulated signaling pathway among cell types. Downregulated neurexin-neuroglin and Glu-GluR interactions were observed in the R306C mutant organoids. **g** Integrated UMAP plot of 3-month cultured RTT-V247X cerebral organoid and isogenic control. Data are reproduced from Fig. 1c. **h** Differential gene expression in cortical organoids carrying MeCP2[V247X] mutation, identifying downregulation of GABAergic receptors in mutant organoids. RNA was extracted and pooled from six different organoids in each condition for bulk RNAseq. The volcano plot shows 896 upregulated and 494 downregulated genes. **i** GABRA4 and GABRA2 expression in different cell types; downregulation was observed in excitatory but not in inhibitory neurons. **j** Inferred neuron-neuron connectivity determined by NeuronChatDB in RTT-V247X mutant and control organoids. **k** Quantification of differential inferred neuron-neuron interaction. Downregulated neurexin-neuroglin and GABA-GABRA4 interactions were observed in the RTT-V247X mutant organoids. **l** Inferred connectivity analysis showing loss of GABA- > GABAR4 directional interaction between excitatory neurons and inhibitory neurons, due to the downregulation of GABARA4 in excitatory neurons. **m**–**o** Drug treatment (CAY10683 (HDAC2 inhibitor) and Baclofen) for 72 hrs for cerebral organoids, showing (**n**) spike frequency. $n = 3$ organoids per condition. $^{*}p < 0.05$, $^{**}p < 0.01$; two-way ANOVA for multiple comparison. Data are presented as mean values ± SD. Data are presented as mean values ± SD. **o** Small-world propensity in the presence of drugs. $n = 3$ organoids per condition. $^{*}p < 0.05$, $^{**}p < 0.01$; two-way ANOVA for multiple comparison. Data are presented as mean values ± SD.

isogenic control organoids (Fig. 6f). In contrast, no significant differences for these types of connectivity were observed in R306C organoids (Fig. 6f). Ca^{2+} imaging was not able to specify the information flow direction, that is, whether E-to-I or I-to-E connectivity was altered; however, scRNAseq and NeuronChatDB indicated that only I to E connectivity was altered, likely due to the downregulation of $GABA_A$ receptors in excitatory neurons in V247X mutant organoids (Fig. 6g, h). Thus, different mutations lead to distinct influences on cell-specific connections.

Discussion

In this paper, we describe altered functional connectivity of neurons and transcriptional changes in RTT patient-derived organoids carrying MeCP2[R306C] and [V247X] mutations. Our findings demonstrate that cortical organoids can recapture developmental maturation of multiple neuron classes (Figs. 1 and 5) along with their alteration by MeCP2 mutations. The two mutations that we examined, both in the TRD, led to some similar but importantly several different outcomes from morphological (Fig. 1), functional (Figs. 2 and 3) and transcriptomic (Fig. 5) perspectives. V247X mutant organoids, but not R306C mutant organoids, were significantly larger and exhibited enhanced proliferation of neural progenitor cells (Fig. 1), confirming previous reports of V247X organoids showing expanded size and rosettes[40]. Here, to enable imaging of neuronal activity[21,25,41], we utilized cortical organoids made with a direct differentiation protocol without Matrigel embedding. Cerebral organoids with Matrigel embedding (which had been used previously) may have resulted in variable volume of the ventricular zone, especially in R306C mutant organoids, due to limited expansion of the epithelial layer in Matrigel[24]. We used a Ca^{2+} sensor together with three-photon microscopy to show that neurons in both R306C and V247X mutant organoids exhibited lower average spike frequency and reduced synchronicity compared to their isogenic pair,

https://doi.org/10.1038/s41467-026-71458-0

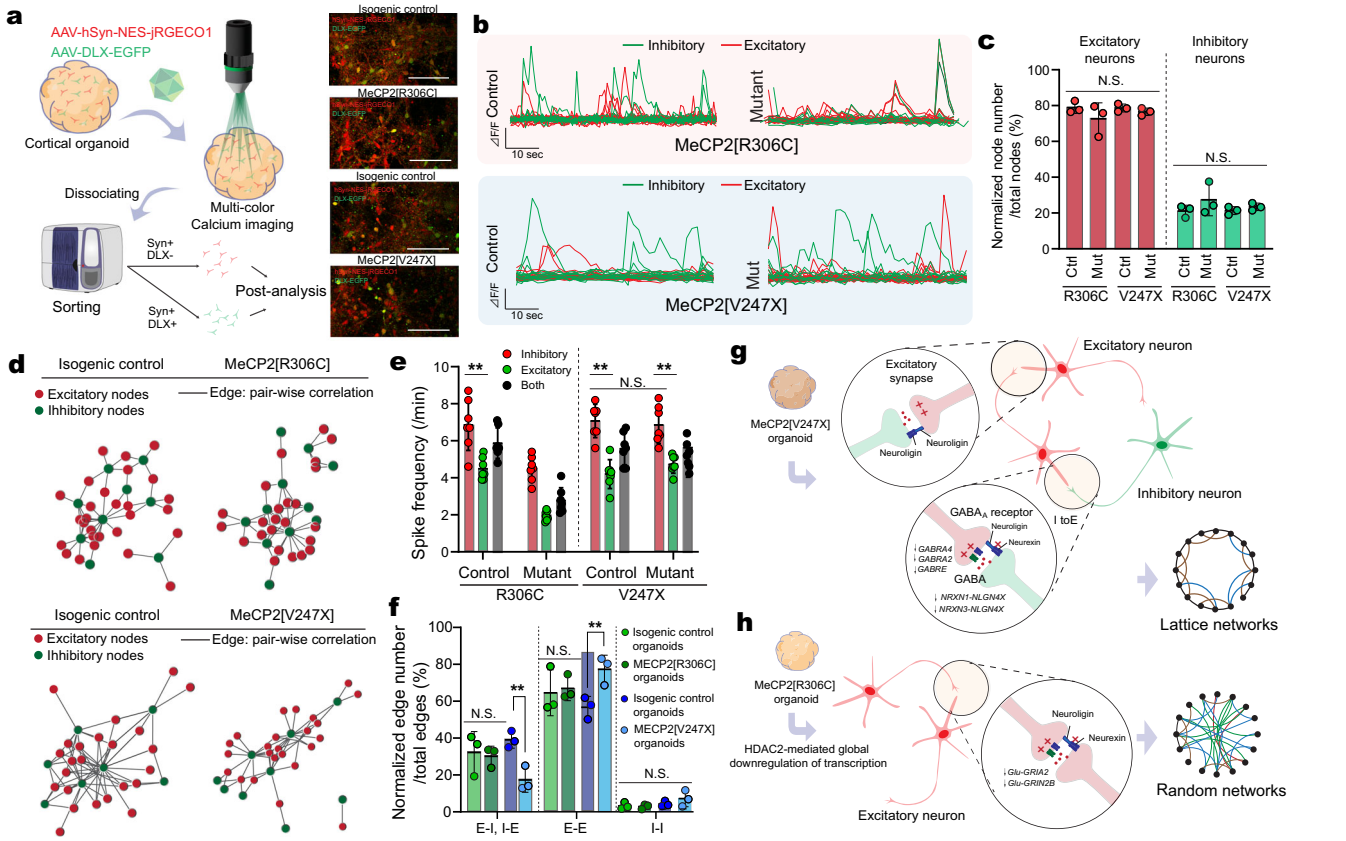

Fig. 6 | DLX labeling combined with Ca^{2+} imaging to determine neuronal activity in excitatory and inhibitory neurons and their networks. a DLX promoter-driven EGFP was co-expressed with jRGECO1a under hSyn promoter to label GABAergic inhibitory neurons 2 weeks prior to imaging. Time-lapse images were acquired by two-photon and three-photon microscopy. After imaging, the cortical organoids were dissociated as single cells and sorted according to Syn + / Dlx- (Excitatory) and Syn + /Dlx+ (Inhibitory) neurons, followed by RNA extraction and PCR. **b** Ca^{2+} imaging of neuronal responses; neurons were clustered into excitatory and inhibitor neurons based on Dlx labeling in post-hoc analyses. **c** Quantification of normalized node number (the number of neurons) in all cortical organoids. $n = 3$ organoids per condition. **d** Representative E/I networks. E/I tags were applied to graph theory analyses for plotting functional networks. Green dots indicate inhibitory nodes and red dots indicate excitatory nodes, which together form one or two modules of networks. **e** Separately calculated spike frequency in inhibitory and excitatory neurons based on labeling information. $n = 6$ organoids per condition. $^*p < 0.05$, $^{**}p < 0.01$; one-way ANOVA. Data are presented as mean values ± SD. **f** Quantification of normalized number of edges for E/I nodes, E/E nodes, and I/I nodes defined from E/I networks. $n = 3$ organoids per condition. $^*p < 0.05$, $^{**}p < 0.01$; one-way ANOVA. Data are presented as mean values ± SD. **g** Schematic of MeCP2[V247X] cortical organoids illustrating altered excitatory–inhibitory (E/I) balance and synaptic organization. Excitatory and inhibitory neurons form structured lattice-like networks along with dysregulation of neuroligin and neurexin and GABA receptor subunits at inhibitory synapses, leading to impaired inhibitory-to-excitatory (I → E) connectivity. **h** Schematic of MeCP2[R306C] organoids showing HDAC2-mediated global transcriptional downregulation predominantly affecting excitatory neurons. Reduced expression of glutamatergic synaptic components, including GRIA2 (GluA2) and GRIN2B (GluN2B), leads to weakened synaptic connectivity and disorganized circuit formation, resulting in random network topology.

indicating disruptions in synaptic connections (Fig. 2). These data are consistent with a previous report of altered neuronal activity in RTT organoids, in particular deficits in the balance of excitatory and inhibitory synapses in MeCP2 mutant cerebral cortex – ganglionic eminence (Cx+GE) fusion organoids, including from a 705delG (same as V247X) mutation[25]. This study further identified the loss of functional connections between excitatory neurons and inhibitory neurons with DLX labeling using calcium imaging.

Graph theory-based functional network analyses demonstrated a greater number of connections per neuron in organoids with both RTT mutations (Fig. 3). These analyses revealed altered functional connectivity and network structures, characterized by changes in the local clustering coefficient and SWP: SWP was highly reduced in R306C organoids compared to controls (Fig. 3). Network analyses of human functional brain activity data have shown that neurons may be efficiently linked by local and long-range connections to represent robust and globally-efficient processing[26]. Our findings demonstrate that even cortical organoids have small-world structure, indicating organized rather than random connectivity, and mutant organoids display disruption of SWP. Additionally, THG imaging allowed us to visualize the laminar structure of organoids alongside Ca^{2+} activity, demonstrating that intra-layer functional connectivity of neurons was more abundant than inter-layer connectivity in control organoids. However, this trend weakened in RTT mutant organoids, especially with the V247X mutation (Fig. 4).

Bulk RNAseq and scRNAseq results followed by NeuronChatDB analysis showed altered gene expression of HDAC2 in neurons in R306C organoids and impaired GABA-A receptor expression in excitatory neurons in V247X organoids (Fig. 5). Treatment with an HDAC2 selective inhibitor and a GABA agonist, respectively, in the two organoid mutations restored neuronal functionality, including spike frequency and SWPs (Fig. 5n, o). HDAC2 is an important transcriptional co-repressor with MECP2, and the R306C mutation has been shown to disrupt the interaction between another class 1 HDAC, HDAC3, and the NCoR interaction domain[42]. This disruption may lead to abnormal HDAC2 gene expression[43], which has previously been implicated in neurodegeneration and brain aging, such as Alzheimer's disease[44–46]. Restoration of HDAC2 levels has been shown to improve neuronal

maturation and reduce amyloid-beta peptide, along with restoring mitochondrial dynamics in Alzheimer's disease[47]. Our findings highlight the temporal limitation of chemical-based inhibitors of HDAC2 to rescue phenotypes, since the restoration can be only applied in narrow windows of time and under specific conditions (Fig. S10) as also commonly observed in the treatment of neurodegenerative diseases or neurodevelopmental disorders[48,49]. Although further assessment and optimization of appropriate time windows is necessary, our results suggest that selective restoration of HDAC2 combined with gene therapy such as CRISPR/dCas9-based epigenetic modulation could be one of the strategies for restoring phenotypes in R306C and other RTT mutations that target similar mechanisms. The V247X mutation causes upregulation of specific miRNAs, especially miR-199 and miR-214, in organoids[40] by mechanisms that include aberrant BMP4 and SMAD signaling[9]. Local miRNA-dependent translational regulation of GABA-A receptor subunits has been described[50], and could represent a mechanism by which V247X mutation-dependent miRNAs downregulate GABA-A receptors. Our findings indicate that MeCP2 dysfunction exerts both mutation-specific and convergent effects in the pathogenesis of RTT, underscoring the need for mutation-specific therapeutic strategies.

By labeling DLX-promoter driven inhibitory neurons with EGFP and using jRGECO1a as a Ca^{2+} indicator, along with fast-scan two-photon microscopy, we identified responses of inhibitory (DLX^{+}) and putative excitatory (DLX^{-}) neurons (Fig. 6). We identified several subtypes of interneurons, including SST-, VIP-, and PVALB-expressing neurons, as a minor but distinct population within the neocortex of cortical organoids, consistent with their emergence during human cortical development[51] (Fig. S3K–M). E-I connectivity exhibited reduced strength while excitatory-excitatory connectivity increased in V247X organoids compared to isogenic controls, whereas no significant differences in connectivity were observed in R306C organoids. Additionally, scRNAseq, NeuronChatDB analysis, and immunofluorescent staining revealed a reduction of I to E connection strength via downregulation of *GABRA2* and *GABRA4* in excitatory neurons and impairment of GABA-GABRA and NRX-NLGN signaling pathways due to the downregulation of *NRXN1*, *NRXN3*, *NLGN4X* in excitatory neurons, which may trigger altered network connectivity and SWP in V247X organoids. These alterations of E/I balance and reduction or loss of connections between excitatory and inhibitory neurons have been shown in RTT model mice[52,53]. In R306C organoids, we observed altered NRX-NLGN interactions, resulting in the loss of synchronization of neuronal activity (Figs. 2f and 5f), which is also observed in RTT mouse models along with the disruption of the assembly of the MeCP2/Rbfox/LASR complex, leading to aberrant splicing of Nrxns and Nlgn, which is critical for synaptic function and plasticity[54]. CellChatDB analysis revealed that astrocyte-to-excitatory neuron communication in V247X organoids was significantly deficient. Specific signaling pathways involving *NRG3-ERBB4, NRXN3-NLGN1*, and *Glu-SLC1A2/3-GLS to GRIAs* were disrupted, also confirmed by downregulation of individual gene expression for GLS and NRG3 in astrocyte and ERBB4 in excitatory and inhibitory neurons, which are fundamental for astrocyte-neuron adhesion and glutamate regulation at the synapse[39,55]. Although further cross-validations with multimodal analysis, including immunostaining with cell-type identification, scRNA-seq, single-cell proteomics[56], or single-cell ribosome profiling[57] to measure translation of protein in individual cells and provide additional layers of validation and mechanistic insight are necessary, these findings add to the evidence that astrocytes have critical, diverse, and mutation-specific roles in the pathophysiology of RTT[58–60].

Preliminary EEG data from human patients carrying truncating [R255X and R270X] or missense [R306C] mutations in the TRD indicated that SWPs were altered compared to age-matched controls in a manner similar to changes observed in organoids with truncating (V247X) or missense (R306C) mutations in the TRD, suggesting that large-scale connectivity changes in RTT patients may originate in early development (Figs. S4 and S5). SWP derived from fMRI measurements is also disrupted in schizophrenia patients[61]. Importantly, our comparison of EEG data from human RTT patients and neuronal activity from cortical organoids spanned different scales of data by applying the same mathematical calculation (SWP). Graph theory-based connectivity analysis, particularly through metrics such as SWP, provides a powerful framework for examining brain network organization across multiple spatial scales[26,27]. This is particularly relevant given the inherently fractal nature of neuronal networks and the well-established scale-free topology observed in brain connectivity. These features suggest that principles governing local microcircuits may also apply at the meso- and macroscale levels of brain organization. In this context, our analytical strategy—grounded in small-world network theory—offers a rational and theoretically supported basis for comparing network architecture across different biological systems, including cerebral organoids and in vivo human brains. Nonetheless, SWP analysis of organoid activity cannot be directly compared to EEG analysis from humans. While this approach provides valuable insights, further in-depth investigation is necessary to clarify how MeCP2 mutations, through disruptions in excitatory-inhibitory (E–I) balance, may alter both local synaptic connectivity and the broader integration of long-range networks in cerebral organoids and human subjects. Our utilization of a cerebral organoid model, combined with multiphoton imaging using Ca^{2+} tracers and cell-specific labeling and transcriptomic analyses, demonstrates a valuable tool for studying the early development of neuronal activity and networks in neurodevelopmental disorders. These findings hold promise for understanding mutation-specific mechanisms of RTT, and developing targeted mutation-specific therapeutics

Methods

Ethics approval

All methods were performed in accordance with the relevant guidelines and regulations. The use of human iPS cells was reviewed and approved by Picower Institute for Learning and Memory, Massachusetts Institute of Technology, through STR-based human cell-line authentication (MIT). The human iPS cells were handled in accordance with approved protocols. All EEG data were collected at Boston Children's Hospital. All relevant ethical guidelines were followed, and all necessary IRB and/or ethics committee approvals were obtained. No subject-identifiable information was included in this work.

RTT patient-derived iPS cells and isogenic controls

RTT patient-derived hiPS cells carrying the heterozygous MECP2[V247X] mutation (female, 25Y, 705 G deletion, frameshift; very rare in RTT patients) and their isogenic control were obtained from the Coriell Institute (WIC07i-07982-4(MT) and WIC07i-07982-2(WT)). The isogenic control cell line had both wild-type and mutant alleles of MECP2, but the mutant allele that had the MECP2 mutation was X-inactivated in all of the mutant cells (Fig. S1A). Another RTT patient-derived hiPS cell line, which carries the heterozygous MECP2[R306C] mutation (female, 8Y, missense; 4–7% of RTT patients), and its isogenic control was obtained from the Coriell Institute (WIC05i-127-325(MT) and WIC04i-127-33(WT)). The isogenic control was established by site-directed genome editing by CRISPR/Cas9 to repair the mutant allele of MECP2, resulting in isogenic control cells having only wild-type alleles of MECP2 (Fig. S1A)[62]. Healthy human iPS cells were also obtained from Coriell Institute (GM23279, female, 36Y) as a non-RTT-related healthy control. All hiPS cells were maintained on Matrigel-coated 6-well plates in mTeSR Plus medium (STEMCELL Technologies) with 10 μM Y-23632 (Rock inhibitor, STEMCELL Technologies) for the first day after each passage and subcultured every 5–7 days using ReLeSR reagent (STEMCELL Technologies). They were characterized by immunostaining with pluripotent markers (OCT3/4, Nanog, TRA-1-60, and

SSEA4), and MECP2 mutations were identified by Sanger sequencing at the DNA level (Fig. 1b), allele-specific PCR (Fig. S1F, E), western blotting (Fig. S1F) and immunostaining of protein expression levels (Fig. S1G). In addition, whole exome sequencing was performed (Germline Whole Exome Sequencing (WES) v6.0., 2 × 150 bp reads, Broad Institute) to determine the MECP2 mutation and confirm the absence of other mutations (Fig. S1D, F). SNVs and indels were characterized by mapping on the reference genome (GRCh37/hg19).

RTT cerebral organoid formation and differentiation

To generate cerebral organoids, two mutant hiPS cell lines and isogenic control iPS cells on 6-well plates were dissociated into single cells with TrypLE Express and then plated at 30,000 cells per well on U-bottom ultra-low attachment 96-well plates (Corning) with mTeSR Plus supplemented with 20 µM of Y-23632. After 24 h, the culture medium was replaced with neural induction medium (knockout DMEM-F12, 15% (v/v) knockout serum replacement, 1% (v/v) MEM-NEAA, 1% (v/v) GlutaMAX, 100 nM LDN-193189, 10 µM SB431542, and 10 µM XAV939) and changed every other day. After 10 days of culture, the culture medium was replaced with 1:1 mixture of knockout DMEM/F12 and neurobasal medium supplemented with 0.5% (v/v) N2 supplement, 1% (v/v) B27 plus supplement with vitamin A, 1% (v/v) GlutaMAX, 1% (v/v) MEM-NEAA, and 2.5 ng/ml (v/v) human insulin solution. This medium was changed every 2 days until 18 days of culture had elapsed. After 18 days, the organoids were transferred to flat-bottom ultra-low attachment 24-well plates (Corning) on a rocking shaker (120 rpm) and switched to a maintenance medium (Neurobasal medium supplemented with 1% (v/v) N2 supplement, 2% (v/v) B27 supplement with vitamin A, 1% (v/v) GlutaMAX, 1% (v/v) MEM-NEAA, 0.25 mg/ml (v/v) human insulin solution, 20 ng/ml BDNF, 200 µM ascorbic acid, 100 µM dibutyryl-cAMP (Sigma-Aldrich), and 1% (v/v) Penicillin/Streptomycin). After 30 days from differentiation, the culture medium was changed twice per week with BrainPhys medium supplemented with 2% (v/v) B27 supplement with vitamin A, 1% (v/v) GlutaMAX, 20 ng/ml BDNF, 20 ng/ml GDNF, and 1%(v/v) Penicillin/Streptomycin until the time of imaging. For the drug treatment experiments, organoids were treated with DL-2-Amino-5-phosphonopentanoic acid (AP5, 100 µM), CNQX;100 µM, and bicuculine 50 µM just before Ca^{2+} imaging. For chronic treatment, organoids were treated with Baclofen 20 µM and HDAC2 selective inhibitor (CAY-10683, Santacruzamate A, 50 µM) for 72 hours prior to imaging.

Virus infection

To visualize neuronal activity by fluorescent Ca^{2+} indicators (GCaMP6f driven by CAG promoter and jRGECO1a driven by hSyn) and to label GABA-ergic interneurons under mDLX enhancer element, the organoids were transfected using AAV1. pAAV.CAG.GCaMP6f.WPRE.SV40 was a gift from Douglas Kim & GENIE Project (Addgene #100836). pAAV.Syn.NES-jRGECO1a.WPRE.SV40 was a gift from Douglas Kim & GENIE Project (Addgene plasmid # 100854; http://n2t.net/addgene:100854; RRID:Addgene_100854). pAAV-mDlx-GFP-Fishell-1 was a gift from Gordon Fishell (Addgene plasmid # 83900; http://n2t.net/addgene:83900; RRID:Addgene_83900). Additionally, 2 µL of AAV solution was added to 500 µL of medium in 24-well plates containing one cerebral organoid at least 1–2 weeks before multi-photon imaging. Then, the maintenance medium was replaced with BrainPhys Imaging Optimized Medium supplemented with 2% (v/v) B27 supplement with vitamin A, 1% (v/v) GlutaMAX, 20 ng/ml BDNF, 20 ng/m l GDNF, and 1% (v/v) Penicillin/Streptomycin before imaging.

Three-photon and two-photon microscope for calcium imaging

To capture Ca^{2+} dynamics of neurons deep within live organoids, three-photon excitation at 1300 nm was used for both GCaMP6f with label-free THG, or co-labeling of jRGECO1a/DLX-EGFP with label-free THG, with a Spirit-NOPA laser system (30-40 fs, Spectra-Physics). A 1300 nm wavelength laser was pumped and compressed from a 1040 nm Spirit One laser (300 fs, 400 kHz, 16 W, Spirit, Spectra-Physics). The laser beams were scanned by a pair of galvo-galvo scanners (6215 H, Cambridge Technologies) to image the laser spot on the back aperture of the objective (Olympus 25×, 1.05 N.A., or Nikon 16×, 0.8 N.A.) using a pair of custom-designed scan and tube lenses. A pair of collection lenses for four photon-multiplying tubes (PMTs) collected the emitted signal from the cerebral organoids. The frame rate at 256×256 pixel resolution was increased up to 5 Hz for functional imaging or 0.9 Hz for structural imaging with 512×512 pixels. All of the fluorescent emission light was initially separated by a primary dichroic short-pass filter mirror (890 nm). GCaMP6f (EGFP) signals were detected using GaAsP photomultiplier tubes (H7422A-40, Hamamatsu, Japan) with a bandpass filter (Semrock, 540/50 nm). jRGECO1a was detected using GaAsP photomultiplier tubes (H7422A-40, Hamamatsu, Japan) and a bandpass filter (Semrock, 610/50 nm). THG signal was detected using a GaAsP photomultiplier tubes (H7422A-40, Hamamatsu, Japan) and a narrow-bandwidth bandpass filter (Semrock, 430/20 nm). The laser power was attenuated by a polarizer down to 10 mW for surface observation and 40-50 mW for deep-tissue observation. Automated image acquisition and control of the scanners and sample stage was carried out using ScanImage (Vidrio)[63]. The organoids were placed on an x-y motorized stage and the objective lens was placed on a single-axis motorized stage (MMBP, Scientifica) to move it in the z-direction.

For some experiments, we used DLX-labeled neurons and Ca^{2+} imaging simultaneously, employing fast scanning. For these, we used a two-photon microscope employing a galvo-resonant scanner (Bruker) with Insight X3 laser (Spectra-Physics) at 1040 nm for jRGECO1a excitation and a MaiTai laser (Spectra-Physics) at 860 nm for EGFP excitation. Both lasers were aligned with the same light path and could be scanned up to 60 Hz sampling frequency at 512×512 resolution. The emission light was initially separated by a primary dichroic short-pass filter mirror (890 nm) and the green and red signals were separated by a dichroic mirror (Semrock, 540/50 nm) and further filtered by bandpass filters (525/25 nm and 610/45 nm, respectively). Both signals were detected using GaAsP photomultiplier tubes (H7422A-40, Hamamatsu, Japan). The microscope and laser were controlled by Prairie View software (Bruker).

Data processing of Ca2+ imaging dataset

Time-lapse calcium imaging data were processed using Suite2p (suite2p, python = 3.9) to identify active neurons. Regions of interest (ROIs) were defined to encompass individual neurons within the field of view. Baseline fluorescence (F_avg) for each ROI was calculated as the average of the bottom 10% percentile of fluorescence intensity values. The relative change in fluorescence over baseline (ΔF/F) was computed as (F - F_avg) / F_avg. A photobleaching correction was implemented by normalizing the ΔF/F trace using the slope obtained from the initial (F_start) and final (F_end) fluorescence values. In experiments involving DLX co-labeling and mosaic organoids, Suite2p was additionally employed to identify and export binary masks corresponding to DLX-positive neurons (identified by EGFP expression) and EGFP-mutant neurons (using a threshold of 0.25). This information, along with ΔF/F and spatial coordinates (x, y) of each neuron, was exported for further analysis. Exported data (delta F, x-y neuron positions, and DLX index) were loaded in MATLAB and further analyzed according to data type. The delta F/F value was deconvolved to identify single neuron activity, and then neuronal spikes were detected by using the "findpeaks" function in MATLAB. The spike frequency was calculated in a specific period of time (minutes). To calculate the undirected graph, network nodes were defined by deconvolved deltaF/F of Ca^{2+} signals, and a continuous measure of association between nodes was estimated based on the correlation or connection probability between neurons. Correlation matrices were generated by compiling all pairwise associations between nodes and applying a

threshold to each element of this matrix to produce a binary adjacency matrix[26]. Finally, the network parameters of interest in these graphical models of the organoid network were calculated and plotted as a structural network that retains geometric information and a functional network that retains topological information determined by the pairwise correlation between neurons. In functional networks, the locations of nodes were calculated by force-directed layout based on the Kamada-Kawai algorithm[28] and Fruchterman-Reingold algorithm[29]. Functional networks were mainly used for the analysis of organoids (Figs. 3 and 4), and structural networks were utilized for EEG analysis (Figs. S4 and S5). For functional analysis, the geometric information (x-y neuron positions) and the layer clustered index (superficial, intermediate, and SVZ/VZ layer) were included. Layer indexes were identified by THG images, which were taken at the same location as the FOVs. Equations to calculate key parameters, including Pearson's pairwise correlation, local clustering coefficient, path length, and SWP, are given below.

Pairwise correlation coefficient. To determine the functional connectivity between two individual neurons x and y, Pearson's pairwise correlation coefficients r_{xy} were calculated after shifting to zero mean based on the following formula.

$$r_{xy} = \frac{\sum_{i=1}^{n}(x_i - \bar{x})(y_i - \bar{y})}{\sqrt{\sum_{i=1}^{n}(x_i - \bar{x})^2}\sqrt{\sum_{i=1}^{n}(y_i - \bar{y})^2}} \quad (1)$$

where n indicates number of time samples and $\bar{x}$ and $\bar{y}$ indicate the average response of neurons x and y.

Local clustering coefficient. The local clustering coefficient denotes the degree to which a vertex's neighbors are connected to one another. We first calculated the local clustering coefficient c_i for each node i as:

$$c_{i,O} = \frac{1}{k_i(k_i-1)}\sum_{j,k}\left(\hat{w}_{ij}\hat{w}_{jk}\hat{w}_{ik}\right)^{1/3} \quad (2)$$

where w_{ij} corresponds to the strength of a connection between nodes i and j, = / ()ˆw w max w_{ij} w_{ij}. w_{ki} correspond to the number of edges connected to nodes i. We thus defined the average clustering coefficient C, to be the average of the local coefficients:

$$C = \frac{1}{N}\sum_i c_i \quad (3)$$

where, N corresponds to the total number of nodes in the network.

Path length. Path length L is the average shortest distances between two nodes i and j, described as

$$L = \frac{1}{N(N-1)}\sum_{i\neq j} d_{ij} \quad (4)$$

where, for a binary network, d_{ij} is the shortest path between nodes i and j. We defined the distance between two nodes as $d_{ij} = 1/w_{ij}$.

Small-world propensity. To quantify the extent to which a network displays small-world structure, we defined the SWP[64], ϕ, to reflect the deviation of a network's clustering coefficient, C_{obs}, and characteristic path length, L_{obs}, from both lattice (C_{latt}, L_{latt}) and random (C_{rand}, L_{rand}) networks constructed with the same number of nodes and the same degree of distribution:

$$\phi = 1 - \sqrt{\frac{\Delta_C^2 + \Delta_L^2}{2}} \quad (5)$$

where

$$\Delta_C = \frac{C_{latt} - C_{obs}}{C_{latt} - C_{rand}} \quad (6)$$

and

$$\Delta_L = \frac{L_{obs} - L_{rand}}{L_{latt} - L_{rand}} \quad (7)$$

The ratios Δ_C and Δ_L represent the fractional deviation of the metric (C_{obs} or L_{obs}) from its respective null model (a lattice or random network). Networks with a high SWP can be categorized into three classes: (i) equally high clustering and low path length (both low Δ_C and Δ_L), (ii) high clustering and moderate path length (low Δ_C and moderate Δ_L) or (iii) moderate clustering and low path length (moderate Δ_C and low Δ_L).

Determination of inter- and intra-layer connections

For label-free determination of the structure of cortical organoids, a three-photon microscope and a THG channel were used, and the structural images were taken on top of functional imaging by GCaMP6f. Image analysis of the THG signal facilitated the extraction of individual neuron coordinates (x, y) within the 2D plane, thereby establishing their spatial distribution. Furthermore, the THG images were utilized to identify the center of rosette structures, a hallmark feature characteristic of the organoid surface. Subsequently, the angular relationship (θ) between each pair of neurons and the rosette center was calculated using the inverse cosine function (cos θ).

Recording and processing of EEG dataset

EEG data from RTT patients and typically-developing subjects were recorded by the EGI NetStation system for data collection at a 1000 Hz sampling rate and downsampled to 256 Hz with 128 channels, and analyzed a 10–20 electrode system for a recording period of 5 min. While recording, subjects sit in front of a monitor in a dimly lit room and watch videos, screen savers-like video (as in the ABC-CT study[65]). The recorded data were first processed with BEAPP to remove line noise and artifacts by ICA[66] and filtered with a 0.1 Hz high-pass filter and notch 60 Hz filter to remove DC noise. We analyzed 10 EEG resting recordings from five RTT patients and 5 typically-developed individuals, aged 3–22 years old. Two RTT patients had a MeCP2 truncating mutation (MeCP2[R255X]), two other patients had a truncating MeCP2[R270X]) mutation, and another patient had a MeCP2 [R306C] SNP mutation. Processed time-series data were first segmented into 2 sec each for a total of 77 epochs, then the power spectrum density was calculated for each of the 10–20 electrodes. In addition, wavelet coherence between 1 and 100 Hz among all combinations of electrodes was calculated in each epoch, and the calculated coherence was used as the weight of connections in the graph analysis. Based on wavelet coherence, topological analysis was performed, and the degree of node, local clustering coefficient, and SWP were calculated in the same way as for Ca^{2+} imaging data from organoids (Figs. S4 and S5).

Microfluidic imaging chamber and temperature control system

To observe organoids in stable conditions under three-photon and two-photon microscopes, a microfluidic device was fabricated to fix the relative position of organoids in a reproducible manner during observation. SU-8 master positive patterned molds were fabricated by

standard photolithography techniques described elsewhere[67]. Briefly, SU-8 (2100) was poured onto a Silicon wafer (6-inches) and spin-coated (1200–1500 rpm, for 30 sec). The wafer was baked for 9 min at 65 °C and 40 min at 95 °C on a hotplate. Then, the wafer was irradiated by UV light (365 nm, 2.5–3.0 mW cm^2) with a photomask for 60–75 sec by Mask Aligner (EV620, TRL EV1). The wafer was baked for 7 min at 65 °C and for 13 min at 95 °C on a hotplate. After the wafer had cooled, SU-8 was developed using SU-8 Developer for 15 min, then washed with isopropyl alcohol (IPA) three times. The wafer was baked for 3 min at 150 °C in the oven. The thickness of the SU-8 was approximately 150 μm. A microfluidic device was made with a polydimethylsiloxane (PDMS) silicone elastomer kit Sylgard184 (Dow Corning). Silicone elastomer and a curing agent were mixed at a weight ratio of 10:1, degassed, poured onto the patterned SU-8 structures, and cured in the oven at 80 °C for 6 h. The holes for retaining cerebral organoids were created with biopsy punches (3 mm), and PDMS devices were sterilized by autoclave.

Reverse-transcription PCR

To measure the biological activity of organoids, total RNA was isolated from tissues with TRIzol (Sigma) combined with Direct-zol RNA Purification Kits (Zymo Research). Reverse transcription was performed using a Superscript VILO cDNA Synthesis Kit (Thermo Fisher Scientific). The primer sequences are shown in Table S2. RT-PCR was performed with QuantStudio 3 (Applied Biosystems) using Takara TB Green Premix Ex Taq II (Takara). The mRNA level of glyceraldehyde 3-phosphate dehydrogenase (GAPDH) was used as the internal standard in all experiments. The RT-PCR experiments were repeated at least three times with cDNAs prepared from separate organoid pools.

Immunostaining and image analysis quantifying axon property

For cryopreservation, cortical organoids were fixed in 4% paraformaldehyde (PFA) and 4% sucrose at 4 °C for 12 h, washed three times with DPBS and transferred to 30% sucrose solution for incubation overnight at 4 °C. Then, organoids were embedded in O.C.T compound (Sakura Finetek) and frozen on a liquid nitrogen-cooled metal block, then sliced for cryosectioning to obtain 15-μm-thick slices (Leica, CM3050). For other organoid immunostaining on Matrigel, organoids were fixed with 4% paraformaldehyde for 1 h and then permeabilized with 0.2% Triton X-100 for 5 min. After blocking with 1% goat serum (Gs) for 2 h, the cells were incubated for 2 h at RT or 4 °C. overnight with a primary antibody. A secondary antibody was then administered for up to 2 h at room temperature. The primary antibodies were mouse monoclonal anti-neuron-specific βIII tubulin (Biolegend, 801202, 1:2000), rabbit monoclonal anti-PAX6 antibody (Abcam, EPR15858, 1:200), rabbit monoclonal anti-human CTIP2 (Abcam, ab18465, 1:200), rabbit polyclonal anti-SATB2 antibody (Abcam, ab34735, 1:100), rabbit monoclonal anti-TBR1 antibody (Thermofisher Scientific, JF10-00), rat monoclonal anti-TBR2(ENOMES) antibody (Thermofisher Scientific, Dan11mag), mouse monoclonal anti-neuroligin 4 antibody (Invitrogen, 14-9158-82, CSTEM30), rabbit polyclonal anti-Neurexin1 antibody (Synaptic system antibodies, 175103), mouse monoclonal anti-Homer1 antibody (Synaptic system antibodies, 160011), rabbit monoclonal anti-Bassoon antibody (Thermofisher Scientific, HL1732), mouse monoclonal anti-GABA antibody (Abcam, ab86186, 5A9), and rabbit monoclonal anti-GABA A receptor alpha subunit4 (NeuroMab clone N398A/34). The secondary antibodies were Alexa Fluor 568 goat anti-rabbit IgG (H + L) (Thermo Fisher Scientific, A11036), Alexa Fluor 488 goat anti-mouse IgG (H + L) (Thermo Fisher Scientific, A11029), and Alexa Fluor 488 goat anti-rat IgG H&L (Abcam, ab150165). Nuclei were stained with Hoechst dye for 20 min at room temperature. Fluorescent images were acquired using a confocal microscope (Olympus, FV1200) with ×20 UPlanSApo objectives (NA: 0.75). To quantify the axon elongation from cortical organoid on Matrigel, all post-image analysis was conducted by using Fiji (http://imagej.nih.gov/ij/). To quantify the axon length and thickness, the axon which are identified by TUJ1-positive features were traced by using the Simple Neurite Tracer plug-in (http://imagej.net/Simple_Neurite_Tracer) in Fiji. The macro command for the axon analysis will be provided upon request.

Flow cytometry and cell sorting

Single cells were dissociated by treatment with TrypLE Express (Thermo Fisher Scientific) or Gentle Cell Dissociation Reagent (Stem Cell Technologies) for 10–15 min. Then, the cell suspension was filtered with a 70-um cell strainer (BD Falcon) in 1% BSA-PBS. To sort inhibitory neurons and excitatory neurons, the cell population was gated by the hSyn-positive population and further gated and sorted as dlx-EGFP-positive neurons (inhibitory neurons) and dlx-EGFP-negative neurons (excitatory neurons) using BD FACSMelody (Fig. S11). After sorting, the total RNA was collected for RT-PCR analysis. All other flow cytometry and analysis were performed with BD FACSMelody or FACSAria and Flowjo.

scRNAseq and processing of transcriptional data

Eight organoids in each condition were dissociated with TypeLE Express for 5–10 min. The cells were then washed with PBS + 0.1% BSA. Multiplexing oligos were incubated for 15 min and washed with PBS + 0.1% BSA three times. The cell suspension was then pooled into one tube and used to perform 10× Chromium followed by sequencing with NovaSeq. Raw sequencing reads were processed using the 10x Genomics CellRanger bioinformatics pipeline v7.2. Cell ranger count matrices of four conditions (isogenic control/ MeCP2[R306C] organoid and isogenic control/ MeCP2[V247X] organoid) were integrated as Seurat objects in Seurat 5 (5.0.1) and Seurat wrapper (0.3.4) in R (4.3.2). Low-quality cells and doublets were removed from the following downstream analysis according to the number of genes (<500 and >7000) and mitochondria percentage (less than 20%). Combined count matrices were normalized and scaled, integrated with CCA algorithm and centered gene-wise, and then underwent dimensionality reduction using principal component analysis (PCA). After visual inspection of the PCA elbow plot, the top 12 PCs were chosen for further analysis. Clustering was performed on the PCs using the shared nearest neighbor algorithm in Seurat to obtain a UMAP plot. Clusters were identified by Louvain algorithm with multilevel refinement performed in Seurat. Unique cluster genes were identified using FindAllMarkers using the Wilcoxon rank-sum test without thresholds. To annotate the cell type, the following genes were used. RGCs cells: *VIM, HOPX, ASCL1, OLIG2, EOMES, ASPM*. Excitatory neurons: *DCX, BCL11A, BCL11B, GRIA1, GRIA2, GRIN2B, GRIN2A, FOXG1, FOXP2, SATB1, SATB2*. Inhibitory lineage: *DLX1, DLX2, DLX5, DLX6, GAD1, GAD2*. Astrocytes: *S100B*, *GFAP*, and *APOE* (Fig. S4). Based on these annotations, five different cell type populations were further clustered for sub-cluster analysis by recomputing the neighbor and dimensional reduction, as well as UMAP plot for Pseudo-bulk RNAseq and pseudotrajectory analysis. Single sample GSEAs were performed with escape R package (1.12.0) with Hallmark gene sets from MSigDB (https://www.gsea-msigdb.org/gsea/msigdb/). Pseudo-bulk RNAseq was performed by FindMarkers with sub-cluster, and statistical significance was calculated by edgeR package (4.0.14) with Wilcoxon rank-sum test and visualized as a volcano plot. FDR was adjusted using the Benjamini-Hochberg method. Pseudo-trajectory was performed with the Monocle 3 package (1. 3. 4). To further characterize these clusters, bulk hallmark pathway analysis was carried out using the ClusterProfiler R package (4.10.1) and enricher with Hallmark gene sets and gene ontology gene sets from MSigDB. Ligand-receptor interaction analysis at the single-cell level was performed using the CellChat R package (2.1.2) and NeuronChat R package. MicroRNA target predictions were performed based on miRPathDB (https://mpd.bioinf.uni-sb.de/).

Bulk RNAseq and processing of transcriptional data

Cells from differentiated organoids (8 organoids) were lysed using TRIzol Isolation Reagent (Thermo Fisher Scientific) and kept at −80 °C until the next step. RNA was extracted and purified with Direct-zol RNA Purification Kits (Zymo Research). PolyA selection and stranded RNAseq library preparations were performed with Illumina Stranded mRNA Pre-kit with rRNA depletion. RNA-sequencing was performed by the Broad Institute Sequencing Platform. 50 M paired-end configuration and read data were mapped to the human reference genome GRCh37/hg19 or the exosome sequenced genome of its cells. Mapped reads were quantified using featureCount. Differential expression was calculated by edgeR package in R, and used to determine significantly altered genes (adjusted p value < 0.01).

Statistical analysis

The reported values are the means of a minimum of three independent experiments. Data are presented as the mean ± SD. For equal variances and normality distribution, a Student's t test was performed. To compare groups at multiple conditions, statistical comparisons were performed using one-way ANOVA, with post-hoc pairwise comparisons carried out using the Tukey–Kramer method. Statistical tests were performed using GraphPad Prism 9 (GraphPad Software, San Diego, CA). p values < 0.05 or p values < 0.01 were considered significant in all cases.

Reporting summary

Further information on research design is available in the Nature Portfolio Reporting Summary linked to this article.

Data availability

All data supporting the conclusions are present in the paper and the supplementary materials. A reporting summary for this article is available as a Supplementary Information file. Read-level data from Whole Exome-seq (Variant call format), bulk RNAseq and scRNAseq (matrices, barcodes, and features), which have been deposited in the National Centre for Biotechnology Information, Gene Expression Omnibus under accession code: GSE318601 and GSE318602. The processed data and imaging data generated in this study have been deposited in Zenodo under accession code (https://doi.org/10.5281/zenodo.18487289). Any additional information required to reanalyze the data reported in this paper is available from the corresponding author upon request. Source data are provided with this paper.

Code availability

The MATLAB for calculating pairwise correlation of neuronal activity and graph theory to compute network analysis, SWP, and EEG data and R code for RNAseq, scRNAseq, CellchatDB, and NeuroChatDB are available from GitHub (https://github.com/TatsuyaOsaki/network-analysis-organoid-imaging). Source data are provided with this paper.

References

1. Lyst, M. J. & Bird, A. Rett syndrome: a complex disorder with simple roots. *Nat. Rev. Genet.* **16**, 261–275 (2015).
2. Samaco, R. C. & Neul, J. L. Complexities of Rett Syndrome and MeCP2. *J. Neurosci.* **31**, 7951–7959 (2011).
3. Chahrour, M. & Zoghbi, H. Y. The story of Rett syndrome: from clinic to neurobiology. *Neuron* **56**, 422–437 (2007).
4. Archer, H. et al. Correlation between clinical severity in patients with Rett syndrome with a p.R168X or p.T158M *MECP2* mutation, and the direction and degree of skewing of X-chromosome inactivation. *J. Med. Genet.* **44**, 148–152 (2007).
5. Cuddapah, V. A. et al. Methyl-CpG-binding protein 2 (MECP2) mutation type is associated with disease severity in Rett syndrome. *J. Med Genet.* **51**, 152–158 (2014).
6. Amir, R. E. et al. Rett syndrome is caused by mutations in X-linked MECP2, encoding methyl-CpG-binding protein 2. *Nat. Genet.* **23**, 185–188 (1999).
7. Cheadle, J. P. et al. Long-read sequence analysis of the MECP2 gene in Rett syndrome patients: correlation of disease severity with mutation type and location. *Hum. Mol. Genet.* **9**, 1119–1129 (2000).
8. Neul, J. L. et al. Specific mutations in methyl-CpG-binding protein 2 confer different severity in Rett syndrome. *Neurology* **70**, 1313–1321 (2008).
9. Ip, J. P. K., Mellios, N. & Sur, M. Rett syndrome: insights into genetic, molecular and circuit mechanisms. *Nat. Rev. Neurosci.* **19**, 368–382 (2018).
10. Kavalali, E. T., Nelson, E. D. & Monteggia, L. M. Role of MeCP2, DNA methylation, and HDACs in regulating synapse function. *J. Neurodev. Disord.* **3**, 250–256 (2011).
11. Good, K. V., Vincent, J. B. & Ausió, J. MeCP2: the genetic driver of Rett syndrome epigenetics. *Front. Genet.* **12**, 620859 (2021).
12. Yusufzai, T. M. & Wolffe, A. P. Functional consequences of Rett syndrome mutations on human MeCP2. *Nucleic Acids Res.* **28**, 4172–4179 (2000).
13. Nan, X. & Bird, A. The biological functions of the methyl-CpG-binding protein MeCP2 and its implication in Rett syndrome. *Brain Dev.* **23**, S32–S37 (2001).
14. Nan, X. et al. Interaction between chromatin proteins MECP2 and ATRX is disrupted by mutations that cause inherited mental retardation. *Proc. Natl. Acad. Sci.* **104**, 2709–2714 (2007).
15. Lyst, M. J. et al. Rett syndrome mutations abolish the interaction of MeCP2 with the NCoR/SMRT co-repressor. *Nat. Neurosci.* **16**, 898–902 (2013).
16. Ebert, D. H. et al. Activity-dependent phosphorylation of MeCP2 threonine 308 regulates interaction with NCoR. *Nature* **499**, 341–345 (2013).
17. Johnson, C. M. et al. Defects in brainstem neurons associated with breathing and motor function in the Mecp2R168X/Y mouse model of Rett syndrome. *Am. J. Physiol. Cell Physiol.* **311**, C895–C909 (2016).
18. Lamonica, J. M. et al. Elevating expression of MeCP2 T158M rescues DNA binding and Rett syndrome–like phenotypes. *J. Clin. Investig.* **127**, 1889–1904 (2017).
19. Collins, B. E. & Neul, J. L. Rett syndrome and MECP2 duplication syndrome: disorders of MeCP2 dosage. *Neuropsychiatr. Dis. Treat.* **18**, 2813–2835 (2022).
20. Lancaster, M. A. et al. Cerebral organoids model human brain development and microcephaly. *Nature* **501**, 373–379 (2013).
21. Trujillo, C. A. et al. Complex oscillatory waves emerging from cortical organoids model early human brain network development. *Cell Stem Cell* **25**, 558–569.e557 (2019).
22. Nakashima, H. et al. MeCP2 controls neural stem cell fate specification through miR-199a-mediated inhibition of BMP-Smad signaling. *Cell Rep.* **35**, 109124 (2021).
23. Gomes, A. R. et al. Modeling Rett syndrome with human patient-specific forebrain organoids. *Front. Cell Dev. Biol.* **8**, https://doi.org/10.3389/fcell.2020.610427 (2020).
24. Yildirim, M. et al. Label-free three-photon imaging of intact human cerebral organoids for tracking early events in brain development and deficits in Rett syndrome. *eLife* **11**, e78079 (2022).
25. Samarasinghe, R. A. et al. Identification of neural oscillations and epileptiform changes in human brain organoids. *Nat. Neurosci.* **24**, 1488–1500 (2021).
26. Bullmore, E. & Sporns, O. Complex brain networks: graph theoretical analysis of structural and functional systems. *Nat. Rev. Neurosci.* **10**, 186–198 (2009).
27. Latora, V. & Marchiori, M. Efficient behavior of small-world networks. *Phys. Rev. Lett.* **87**, 198701 (2001).

28. Kamada, T. & Kawai, S. An algorithm for drawing general undirected graphs. *Inf. Process. Lett.* **31**, 7–15 (1989).
29. Fruchterman, T. M. J. & Reingold, E. M. Graph drawing by force-directed placement. *Softw. Pract. Exp.* **21**, 1129–1164 (1991).
30. Bonifazi, P. et al. GABAergic hub neurons orchestrate synchrony in developing hippocampal networks. *Science* **326**, 1419–1424 (2009).
31. van den Heuvel, M. P. & Sporns, O. Network hubs in the human brain. *Trends Cogn. Sci.* **17**, 683–696 (2013).
32. Tidball, A. M. et al. Deriving early single-rosette brain organoids from human pluripotent stem cells. *Stem Cell Rep.* **18**, 2498–2514 (2023).
33. Sit, T. P. H. et al. MEA-NAP: a flexible network analysis pipeline for neuronal 2D and 3D organoid multielectrode recordings. *Cell Rep. Methods* **4**, https://doi.org/10.1016/j.crmeth.2024.100901 (2024).
34. Portnova, G., Neklyudova, A., Voinova, V., and Sysoeva, O. Clinical EEG of Rett syndrome: group analysis supplemented with longitudinal case report. *J. Pers. Med.* **12**, https://doi.org/10.3390/jpm12121973 (2022).
35. Jin, S. et al. Inference and analysis of cell-cell communication using CellChat. *Nat. Commun.* **12**, 1088 (2021).
36. Zhao, W., Johnston, K. G., Ren, H., Xu, X. & Nie, Q. Inferring neuron-neuron communications from single-cell transcriptomics through NeuronChat. *Nat. Commun.* **14**, 1128 (2023).
37. Flott, B. & Seifert, W. Characterization of glutamate uptake systems in astrocyte primary cultures from rat brain. *Glia* **4**, 293–304 (1991).
38. Anderson, C. M. & Swanson, R. A. Astrocyte glutamate transport: review of properties, regulation, and physiological functions. *Glia* **32**, 1–14 (2000).
39. Okabe, Y. et al. Alterations of gene expression and glutamate clearance in astrocytes derived from an MeCP2-null mouse model of Rett syndrome. *PLoS One* **7**, e35354 (2012).
40. Mellios, N. et al. MeCP2-regulated miRNAs control early human neurogenesis through differential effects on ERK and AKT signaling. *Mol. Psychiatry* **23**, 1051–1065 (2018).
41. Miura, Y. et al. Generation of human striatal organoids and cortico-striatal assembloids from human pluripotent stem cells. *Nat. Biotechnol.* **38**, 1421–1430 (2020).
42. Nan, X. et al. Transcriptional repression by the methyl-CpG-binding protein MeCP2 involves a histone deacetylase complex. *Nature* **393**, 386–389 (1998).
43. Heckman, L. D., Chahrour, M. H. & Zoghbi, H. Y. Rett-causing mutations reveal two domains critical for MeCP2 function and for toxicity in MECP2 duplication syndrome mice. *eLife* **3**, e02676 (2014).
44. Mahady, L. et al. HDAC2 dysregulation in the nucleus basalis of Meynert during the progression of Alzheimer's disease. *Neuropathol. Appl. Neurobiol.* **45**, 380–397 (2019).
45. Panikker, P. et al. Restoring Tip60 HAT/HDAC2 balance in the neurodegenerative brain relieves epigenetic transcriptional repression and reinstates cognition. *J. Neurosci.* **38**, 4569–4583 (2018).
46. Gräff, J. et al. An epigenetic blockade of cognitive functions in the neurodegenerating brain. *Nature* **483**, 222–226 (2012).
47. Frankowski, H. et al. Knockdown of HDAC2 in human induced pluripotent stem cell derived neurons improves neuronal mitochondrial dynamics, neuronal maturation and reduces amyloid beta peptides. *Int. J. Mol. Sci.* **22**, 2526 (2021).
48. Sun, X.-Y. et al. HDAC2 hyperexpression alters hippocampal neuronal transcription and microglial activity in neuroinflammation-induced cognitive dysfunction. *J. Neuroinflamm.* **16**, 249 (2019).
49. Shukla, S. & Tekwani, B. L. Histone deacetylases inhibitors in neurodegenerative diseases, neuroprotection and neuronal differentiation. *Front. Pharmacol.* **11**, 537 (2020).
50. Rajgor, D. et al. Local miRNA-dependent translational control of GABA(A)R synthesis during inhibitory long-term potentiation. *Cell Rep.* **31**, 107785 (2020).
51. Letinic, K., Zoncu, R. & Rakic, P. Origin of GABAergic neurons in the human neocortex. *Nature* **417**, 645–649 (2002).
52. Li, W. Excitation and Inhibition Imbalance in Rett syndrome. *Front. Neurosci.* **ume 16**, 2022 (2022).
53. Banerjee, A. et al. Jointly reduced inhibition and excitation underlies circuit-wide changes in cortical processing in Rett syndrome. *Proc. Natl. Acad. Sci.* **113**, E7287–E7296 (2016).
54. Jiang, Y. et al. Rett syndrome linked to defects in forming the MeCP2/Rbfox/LASR complex in mouse models. *Nat. Commun.* **12**, 5767 (2021).
55. Sun, J. et al. Mutations in the transcriptional regulator MeCP2 severely impact key cellular and molecular signatures of human astrocytes during maturation. *Cell Rep.* **42**, 111942 (2023).
56. Bennett, H. M., Stephenson, W., Rose, C. M. & Darmanis, S. Single-cell proteomics enabled by next-generation sequencing or mass spectrometry. *Nat. Methods* **20**, 363–374 (2023).
57. VanInsberghe, M., van den Berg, J., Andersson-Rolf, A., Clevers, H. & van Oudenaarden, A. Single-cell Ribo-seq reveals cell cycle-dependent translational pausing. *Nature* **597**, 561–565 (2021).
58. Kahanovitch, U., Patterson, K. C., Hernandez, R., and Olsen, M. L. Glial dysfunction in MeCP2 deficiency models: implications for Rett syndrome. *Int. J. Mol. Sci.* **20**, https://doi.org/10.3390/ijms20153813 (2019).
59. Jin, X.-R., Chen, X.-S., and Xiao, L. (2017). MeCP2 deficiency in neuroglia: new progress in the pathogenesis of Rett syndrome. *Front. Mol. Neurosci.* **10**, https://doi.org/10.3389/fnmol.2017.00316 (2017).
60. Caldwell, A. L. M. et al. Aberrant astrocyte protein secretion contributes to altered neuronal development in multiple models of neurodevelopmental disorders. *Nat. Neurosci.* **25**, 1163–1178 (2022).
61. Liu, Y. et al. Disrupted small-world networks in schizophrenia. *Brain* **131**, 945–961 (2008).
62. Ananiev, G., Williams, E. C., Li, H. & Chang, Q. Isogenic pairs of wild type and mutant induced pluripotent stem cell (iPSC) lines from Rett syndrome patients as in vitro disease model. *PLoS One* **6**, e25255 (2011).
63. Pologruto, T. A., Sabatini, B. L. & Svoboda, K. ScanImage: flexible software for operating laser scanning microscopes. *Biomed. Eng.* **2**, 13 (2003).
64. Muldoon, S. F., Bridgeford, E. W. & Bassett, D. S. Small-world propensity and weighted brain networks. *Sci. Rep.* **6**, 22057 (2016).
65. McPartland, J. C. et al. The autism biomarkers consortium for clinical trials (ABC-CT): scientific context, study design, and progress toward biomarker qualification. *Front. Integr. Neurosci.* **14**, 16 (2020).
66. Levin, A. R., Méndez Leal, A. S., Gabard-Durnam, L. J., and O'Leary, H. M. BEAPP: the batch electroencephalography automated processing platform. *Front. Neurosci.* **12**, https://doi.org/10.3390/ijms20153813 (2019).
67. Ko, Y. J., Maeng, J. H., Hwang, S. Y. & Ahn, Y. Design, fabrication, and testing of a microfluidic device for thermotaxis and chemotaxis assays of sperm. *SLAS Technol.* **23**, 507–515 (2018).

Acknowledgements

We would like to thank Dr. Ritu Raman and Dr. Sina Kheiri at Mechanical Engineering, MIT, for generously allowing us to use the super-resolution confocal microscope (Nikon AX R with NSPARC), which was instrumental for this work. We thank the Koch Institute's Robert A. Swanson (1969) Biotechnology Center for technical support, specifically Microscopy, and FlowCytometry core. We also thank Genome Technology Core at Whitehead Institute for Biomedical Research for Next-Generation sequencing on the Illumina for scRNAseq. We thank Taylor

Johns for editorial assistance, and members of the Sur lab for discussions and advice. This work was supported by NIH grants R01MH085802 and R01NS130361, MURI grant W911NF2110328, the Picower Institute Innovation Fund, and the Simons Foundation Autism Research Initiative through the Simons Center for the Social Brain to M.S.; and Postdoctoral fellowships from the Promotion of Science (JSPS) Overseas Research Fellowships and the Uehara Memorial Foundation Postdoctoral Fellowship to Y.O.; and NIH grant P50HD105351 to A.L. Equipment used for EEG was provided by the University of Tokyo International Research Center for Neurointelligence (WPI-IRCN; to Takao Hensch): and NIH grant P50HD1053 and WPI-IRCN (JSPS) to M.F.

Author contributions

T.O. and M.S. conceived and designed the experiments. T.O. performed the experiments, and T.O. and Y.O. analyzed the data. T.O. applied models to describe biological data and produced the analyses and figures. T.O. and C.D. established organoid lines. D.K., A.L., M.F., and C.N. provided EEG data. T.O. and M.S. wrote the manuscript.

Competing interests

The authors declare no competing interests.

Additional information

Supplementary information The online version contains supplementary material available at https://doi.org/10.1038/s41467-026-71458-0.

Correspondence and requests for materials should be addressed to Tatsuya Osaki or Mriganka Sur.

Peer review information *Nature Communications* thanks Nael Nadif Kasri, Hideya Sakaguchi, and the other, anonymous, reviewer(s) for their contribution to the peer review of this work. A peer review file is available.

Tatsuya Osaki[1,2] ✉, Chloe Delepine[1], Yuma Osako[1], Devorah Kranz[3,4], April Levin[5,6], Charles Nelson[3,4,7], Michela Fagiolini[6,8,9] & Mriganka Sur[1,10] ✉

[1]Picower Institute for Learning and Memory, Massachusetts Institute of Technology, Cambridge, MA, USA. [2]Whitehead Institute for Biomedical Research, Massachusetts Institute of Technology, Cambridge, MA, USA. [3]Division of Developmental Medicine, Boston Children's Hospital, Boston, MA, USA. [4]Department of Pediatrics, Harvard Medical School, Cambridge, MA, USA. [5]Graduate School of Education, Harvard University, Boston, MA, USA. [6]F.M. Kirby Neurobiology Division, Boston Children's Hospital, Boston, MA, USA. [7]Department of Brain and Cognitive Sciences, Massachusetts Institute of Technology, Cambridge, MA, USA. [8]Department of Neurology, Boston Children's Hospital, Boston, MA, USA. [9]Harvard Medical School, Boston, MA, USA. [10]International Research Center for Neurointelligence, The University of Tokyo, Institutes for Advanced Study, Tokyo, Japan. ✉e-mail: osaki@mit.edu; msur@mit.edu